Lin *et al. Journal of Nanobiotechnology* (2025) 23:189
https://doi.org/10.1186/s12951-025-03270-9

Journal of Nanobiotechnology

RESEARCH **Open Access**

Microenvironment-responsive NIR-IIb multifunctional nanozyme platform for bacterial imaging and specialized anti-anaerobic bacteria periodontal therapy

Suai Lin[1,2], Tiehan Cui[1,2†], Yuxin Jiang[3†], Jialiang Xie[3,4], Da Zhong[3,4], Junkai Jiang[1,3], Dan Deng[3,4], Mengzhen Zhao[3,4], Chengzhou Xue[3], Shiyu Gan[3], Jiaxuan Qiu[1,2*] and Xiaolei Wang[3,4*]

Abstract

Periodontitis is a chronic inflammatory disease caused by plaque. In order to remove pathogens and promote tissue repair, the following steps need to be taken simultaneously: localizing the diseased area, improving the anaerobic microenvironment, as well as addressing the anti-inflammatory and osteogenic needs. This study aims to address these issues by developing a responsive near-infrared-IIb nanozyme system (DMUP), assembled from lanthanide-doped down-converted nanoparticles and multi-enzymatically active nanozyme. DMUP binds to bacterial membranes *via* the bacterial targeting peptide ubiquicidin$_{29\text{-}41}$ (UBI$_{29\text{-}41}$). Upon responding to the inflammatory microenvironment, it releases manganese (Mn) nanozyme and paeonol (Pae), and localized infected areas by fluorescent bacterial imaging in the near-infrared IIb (NIR-IIb) region. In particular, the released Mn nanozyme reacts with hydrogen peroxide in the inflammatory microenvironment to generate oxygen (O_2) in situ, thereby improving the anoxic environment to inhibit anaerobic bacteria. On the other hand, as a metal oxide nanozyme, Mn nanozyme scavenges reactive oxygen species (ROS) by mimicking the cascade process of superoxide dismutase and catalase. The phenolic antioxidant Pae shifts macrophages from pro-inflammatory (M1-type) to anti-inflammatory (M2-type) through the Akt/mTOR pathway. It can synergize with Mn nanozyme to regulate the inflammatory microenvironment, thereby reducing inflammation, promoting osteogenic genes expression, and accelerating periodontal tissues regeneration.

[†] Tiehan Cui and Yuxin Jiang contributed equally to this work.

*Correspondence:
Jiaxuan Qiu
qiujiaxuan@163.com
Xiaolei Wang
wangxiaolei@ncu.edu.cn

Full list of author information is available at the end of the article

Graphical abstract

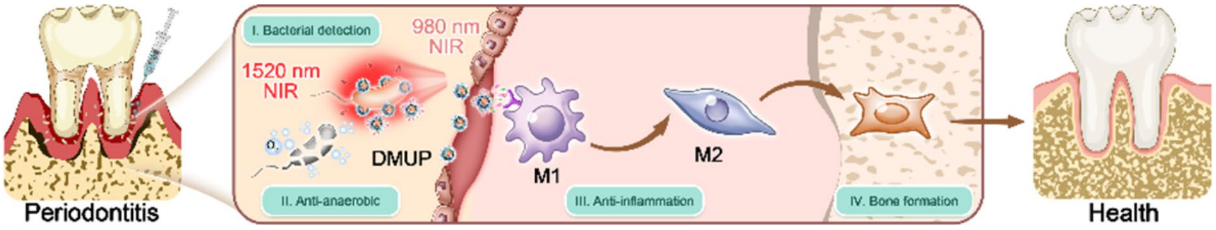

Keywords Periodontitis, Anti-anaerobic, Anti-inflammation, Autophagy, Near-infrared-IIb region imaging

Introduction

Periodontitis, a chronic inflammatory disease caused by plaque [1], has become the sixth most common chronic disease, affecting 734 million people in the world [2]. Typically, periodontitis treatment involves subgingival scaling and root planning (SPR) and antibiotics [3]. However, the periodontal pockets have a complex structure and are covered with soft tissue, which makes it challenging to accurately define the infected area during curettage. As a result, the removal effect of SPR is seriously affected. *Porphyromonas gingivalis* (*P. gingivalis*) is an anaerobic bacterium that causes periodontitis [4]. Moreover, it is also difficult to inhibit such strains in the hypoxic periodontal pocket area by broad-spectrum antibiotics (e.g., minocycline, MC, clinical drug commonly used in periodontitis). Periodontitis progression also relates to the host immune response, which is overactivated with the increase of pathogenic bacteria and their metabolites [5] This immune stress triggers a series of antibody responses that modify the periodontal microenvironment by exacerbating hypoxia [6–8], as well as increasing reactive oxygen species (ROS) and inflammatory factors [9–11]. The imbalanced periodontitis microenvironment further leads to tissue acidification, which in turn affects immune cell function and accelerates tissue damage [12]. These complex interactions further reduce the effectiveness of conventional treatments. Therefore, it is crucial to develop a treatment strategy for periodontitis that includes bacterial visualization (localization of the diseased area), inhibition of anaerobic bacteria, and improvement of the inflammatory microenvironment.

With the advantages of safety, real-time monitoring, non-invasiveness, and deep tissue penetration, the near-infrared-II (NIR-II, wavelength 1000–1700 nm) region fluorescence imaging is an emerging biomedical imaging method [13]. In particular, due to their high chemical stability, excellent photostability, and narrow emission band performance, lanthanum-doped NIR-IIb (wavelength 1500–1700 nm) down-conversion nanoparticles (DCNPs) have attracted significant attention in tumor imaging [14–16]. Thus, when combined with suitable bacterial-targeting ligands, this material could be potentially utilized for the visual localization of infected regions [17–19]. For example, by using the bacteria-targeting peptide ubiquicidin (UBI_{29-41}), the electrostatic adsorption with phosphatidylglycerol (PG) on the bacterial cytosol membrane can effectively increase the recognition of bacteria by the imaging group [20, 21]. The oral cavity is an open environment with diverse dynamics. Therefore, the microenvironmental characteristics of bacteria or diseases can also be used to construct an auto-responsive fluorescence system. This strategy can improve the imaging specificity of pathogenic bacteria in the lesion area and localize the bacterial infection area [22, 23]. Notably, few studies have used bacterial fluorescent probes to image bacteria in periodontal pockets. The high hydrogen peroxide (H_2O_2) content, as well as the acidic microenvironment in the inflammatory tissues, could be utilized to develop responsive fluorescent probes. Thus, the efficiency of bacterial removal during scaling procedures can be potentially improved by constructing a responsive fluorescence imaging platform based on DCNPs to visualize bacteria in periodontal pockets.

After achieving precise imaging, another focus of the therapeutic system is to improve the microenvironment (hypoxia and inflammation) in the infected area. With catalase (CAT)-like activity [24], manganese (Mn) nanozyme catalyzes the disproportionation of H_2O_2 to produce oxygen (O_2). This reaction leads to a significant improvement in the hypoxic microenvironment, which restricts the anaerobic bacterial electron transport chain and inhibits the anaerobic bacteria [25, 26]. Mn nanozyme also possesses superoxide dismutase (SOD)-like activity, which scavenges another ROS (superoxide anion, $\cdot O_2^-$). Thus, it is able to act as an exogenous ROS scavenger, thereby modulating immune-inflammatory products, protecting the endogenous antioxidant system to alleviate the inflammatory response of tissues [27, 28]. By forming an antioxidant system (Mn nanozyme-Pae) with natural antioxidants such as paeonol (Pae) [29], this approach increases cellular autophagic flux and alters the functional morphology of immune cells by targeting intracellular lysosomes. This ameliorates the immune microenvironment to promote an inflammatory environment conducive to osteogenesis, thus achieving the desired therapeutic effect of anti-inflammation and osteogenesis.

This study developed a responsive NIR-IIb multifunctional nanozyme system (β-NaErF$_4$:Yb^{3+}@NaLuF$_4$@mSiO$_2$-Mn-UBI$_{29-41}$-Pae, DMUP), which is capable of responding to multiple stimuli to realize bacterial imaging and inflammatory microenvironment modulation in the periodontitis microenvironment. With Er^{3+} and Yb^{3+} doped NaF nanocrystals as the core, the system was coated with mesoporous silica (mSiO$_2$) to enhance hydrophilicity. Furthermore, the zeolite imidazole skeleton (ZIF-8) metal frame was utilized to precipitate Mn nanozyme in the pores of mSiO$_2$. Subsequently, the system was grafted with bacterial-targeting ligand UBI$_{29-41}$ on its surface and loaded with Pae (Fig. 1). The resultant system demonstrated the following advantages: (1) **Bacterial imaging**. Aggregation of DCNPs and Mn nanozyme produced a fluorescence resonance energy transfer (FRET) effect leading to NIR-IIb fluorescence quenching [30]. Thus, under normal conditions, the DMUP nanoparticles exhibited a fluorescence-quenching state. However, under acidic inflammatory conditions, the hydrogen ions (H$^+$) protonated the ligands in ZIF-8, thereby disrupting the metal-organic framework and releasing Mn nanozyme and Pae from the pores [31, 32]. The released Mn nanozyme and Pae rapidly restored and turned on the NIR-IIb fluorescence of DMUP. Furthermore, by utilizing the targeting property of UBI$_{29-41}$, DMUP bound to the bacterial surface with specificity to achieve fluorescence localization in the infected area (Fig. 1 I). (2) **Anti-anaerobic bacteria**. The released Mn nanozyme reacted with the abundant H$_2$O$_2$ and H$^+$ in the acidic periodontitis environment to generate O$_2$ [33, 34], which effectively inhibited the growth of pathogenic anaerobic bacteria (Fig. 1 II). (3) **ROS scavenging and anti-inflammation**. Mn nanozyme is known to provide CAT-like and SOD-like enzyme activities [27, 28]. It exhibited anti-inflammatory effects by scavenging ROS and reducing tissue inflammation through inhibiting the expression of inflammatory factors (Fig. 1 III). (4) **Promoting bone regeneration**. By using Pae to target lysosomes, the system increased the cellular autophagic flux [29, 35], thereby promoting the transition of macrophages from M1-type to M2-type. This adjustment of the immune microenvironment reduced inflammation and created an environment favorable for tissue repair and regeneration. Consequently, bone matrix proteins were protected, thereby maintaining osteoblast function and activity, which promoted bone regeneration (Fig. 1 IV) [36, 37]. In summary, the multifunctional nano-system DMUP integrated bacterial imaging with anti-anaerobic, anti-inflammatory, and bone regeneration-promoting properties, demonstrating its potential applications in periodontitis treatment.

Methods

Synthesis of the core structure of DCNPs

The composition followed a reported scheme with slight modifications [38]. First, lanthanum acetate [1.0 mmol, Re(CH$_3$CO$_2$)$_3$ (Re = Er/Yb = 8/2)] was added to a flask containing oleic acid (OA, 6 mL) and 1-octadecene (ODE, 15 mL), heated to 150 ℃ to remove water. After cooling to room temperature (RT), a methanol solution of ammonium fluoride (NH$_4$F, 4.0 mmol) and sodium hydroxide (NaOH, 2.5 mmol) was added, followed by stirring for 30 min at 50 ℃. Subsequently, the temperature was raised to 120 ℃ to remove the methanol, and then rapidly heated to 300 ℃ in an argon atmosphere and kept for 50 min. After cooling to RT, ethanol was added to precipitate the DCNPs, which were centrifuged (11000 rpm, 10 min). The product (DCNPs) was dispersed in 20 mL of cyclohexane for further use.

Synthesis of core-shell (DCNPs) structures

The core-shell DCNPs were synthesized by a seed-induced growth method, and prepared by the same co-precipitation procedure. Typically, 1 mmol lutetium (III) acetate hydrate (Lu(CH$_3$CO$_2$)$_3$·xH$_2$O) was added to a solution containing ODE (15 mL) and OA (6 mL) in a 100 mL three-necked flask. The mixture was then heated to 150 ℃ for 30 min to form a clear solution. Subsequently, 4 mL of β-NaErF$_4$:Yb cyclohexane solution was added to the mixed solution, stirred at 70 ℃ for 20 min, and cooled to room temperature. Next, 10 mL of a methanol solution containing 4 mmol NH$_4$F and 2.5 mmol NaOH was added and stirred at 50 ℃ for 30 min. Then, the temperature was raised to 120 ℃ for 30 min for methanol removal. Subsequently, the system was heated to 300 ℃ for 50 min in an argon atmosphere, and after cooling to RT, the core-shell nanocrystals were precipitated with ethanol and dispersed in 20 mL of cyclohexane.

Preparation of DCNPs@mSiO$_2$-COSR (DCMS-COSR)

DCNPs@mSiO$_2$ were prepared using the inverse micellar method and modified with surface carboxylation. A 0.2 g cetyltrimethylammonium bromide (CTAB) was prepared in 30 mL deionized water solution, then 2 mL DCNPs solution was added, and stirred in a water bath at 80 ℃ until clarified, followed by ultrasound for 24 h. A 50 μL mixed solution of TEOS and Carboxyethylsilanetriol sodium salt (CHNaOSi, molar ratio of 1:1) in ethanol (10 mL) was configured. The sonicated mixed solution was placed in a 70 ℃ water bath, and the TEOS/CHNaOSi mixed solution was added dropwise, and the reaction was

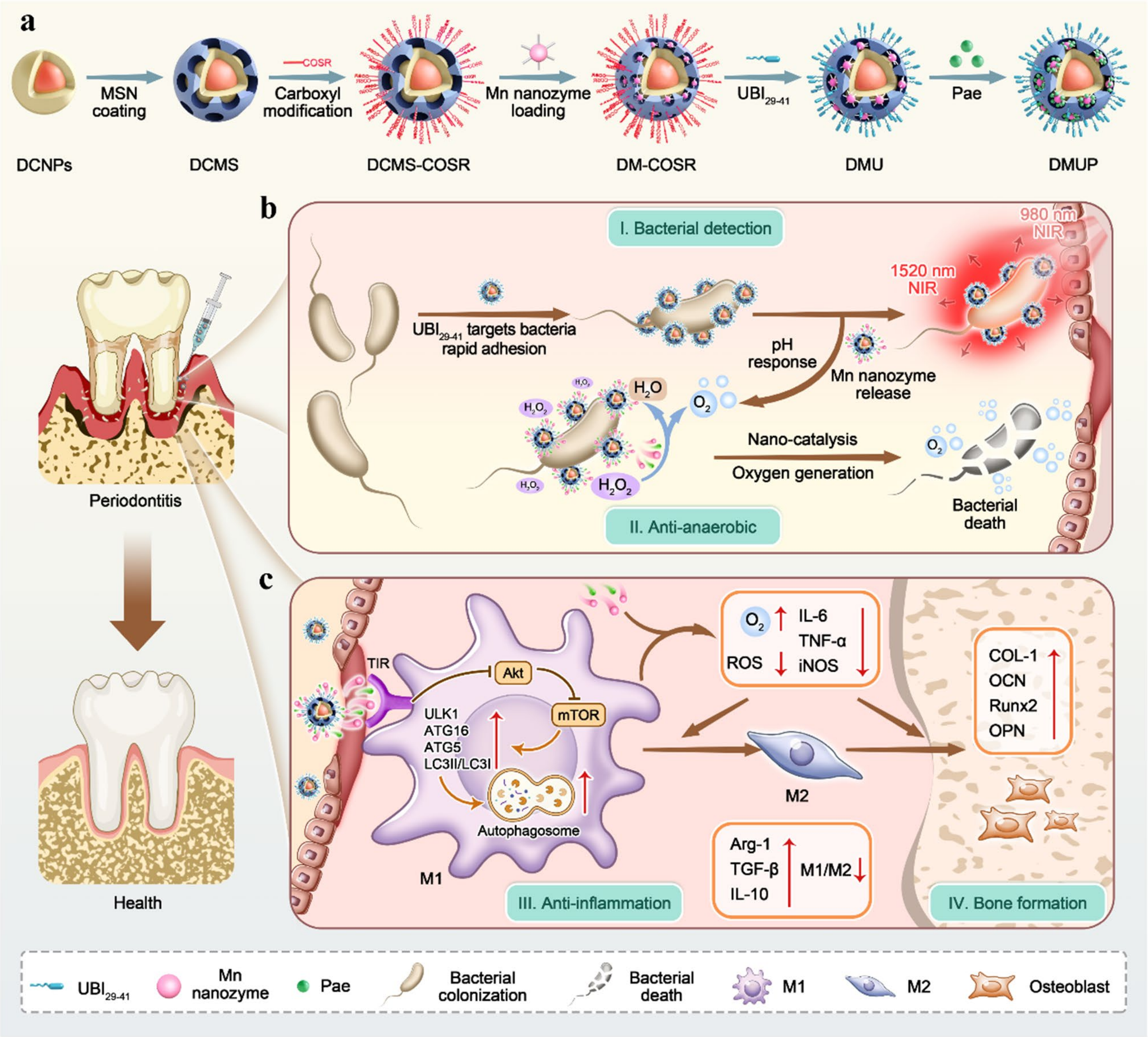

Fig. 1 Schematic structure and working principle of DMUP. (**a**) Down-conversion nanoparticles containing rare earth Er were coated with $mSiO_2$ and surface-grafted with the bacterial targeting ligand UBI_{29-41} to form DCMS-UBI. Through the scaffolding of a metal-organic framework, there was intra-pore precipitation of Mn nanozyme (DMU). The remaining pores were loaded with Pae, a traditional Chinese medicine monomer with anti-inflammatory and immune-modulatory properties to form DMUP. (**b**) DMUP targeted bacterial membranes while the metal-organic framework disintegrated in a low-pH inflammatory microenvironment, thereby releasing Mn nanozyme and restoring NIR-IIb fluorescence properties. This was utilized for bacterial imaging. The released Mn nanozyme catalyzed endogenous H_2O_2 to produce O_2, which inhibited anaerobic bacteria. (**c**) The released Mn nanozyme and Pae acted as an antioxidant system to inhibit the macrophage Akt/mTOR pathway, increased autophagic activity, and promoted macrophage transformation to the M2 anti-inflammatory type. Furthermore, Mn nanozyme scavenged ROS and produced O_2, synergistically improving the periodontitis microenvironment and promoting the regeneration of periodontal bone tissue. DCNPs: $NaErF_4$:Yb@$NaLuF_4$; DCMS: DCNPs@$mSiO_2$; DCMS-COSR: DCNPs@$mSiO_2$-COSR; DM-COSR: DCMS-MnO_2-COSR; DMU: DCMS-MnO_2-UBI_{29-41}; DMUP: DCMS-MnO_2-UBI_{29-41}-Pae

maintained for 6 h to coat the DCNPs surface with carboxyl-functionalized $mSiO_2$ (DCNPs@$mSiO_2$-COOH). Subsequently, the products were washed using anhydrous ethanol, 1 wt% NaCl methanol solution was used to remove the remaining CTAB from the products, and finally anhydrous ethanol was used to wash the products again before they were lyophilized and set aside.

Take 100 mg DCNPs@$mSiO_2$-COOH, 40 mg HOBT, and 42 mg EDC, respectively, and dissolve in 5 mL of deionized water. After magnetic stirring for 0.5 h, centrifugation to precipitate, re-dissolved in 10 mL of 50% ethanol solution (anhydrous ethanol: deionized water = 1:1). Then, add 64 µL of Benzyl Mercaptan, magnetic stirring for 1 h. Next, perform centrifugal precipitation, lyophilization, and storage. Finally, UBI_{29-41} was grafted onto the surface of the DCNPs@mSiO$_2$-COSR (DCMS-COSR).

Synthesis of DCNPs@mSiO$_2$-Mn-COSR (DM-COSR)

Metal-organic frameworks of ZIF-8 were synthesized in DCMS-COSR pores. First, 2-methylimidazole was loaded inside the DCMS-COSR pores by taking 200 mg of 2-methylimidazole completely dissolved in 3 mL of deionized water. And 100 mg of DCMS-COSR was taken and dissolved in 2 mL of deionized water. The above solutions were mixed and stirred magnetically for 2 h. The precipitate was collected by centrifugation and re-dissolved in 3 mL of deionized water. Then, 25 mg of Zinc nitrate hexahydrate ($Zn(NO_3)_2{\cdot}6H_2O$) was dissolved in 2 mL of deionized water, mixed with the above solution, centrifuged with magnetic stirring for 1 h to collect the precipitate, and re-dissolved in 3 mL of deionized water. Subsequently, Mn nanozyme was attached to the ZIF-8 metal frame in the wells. 0.25 mg of potassium permanganate ($KMnO_4$) was dissolved in 1 mL of deionized water, and mixed with the above solution. The precipitate was collected by centrifugation with magnetic stirring for 30 min, and the product was lyophilized to obtain the DM-COSR.

Synthesis of DCNPs@mSiO$_2$-Mn-UBI_{29-41} (DMU)

A total of DM-COSR (50 mg) and UBI_{29-41} (0.1 mg) were used for the reaction, stirred at 4 ℃ for 24 h, centrifuged to precipitate, lyophilized to collect the product (DMU), and stored at 4 ℃.

Synthesis of Pae-loaded DMUP

A mixture of DMU (1.0 mg mL^{-1}) with Pae/ethanol solution (4.0 mg mL^{-1}) was stirred in a light-blocking vial at RT for 24 h. The mixture was centrifuged to obtain the supernatant and the absorbance of the supernatant was measured. A calibration curve for Pae was plotted based on the absorbance at 203.6 nm of a UV-2600 spectrophotometer under the same conditions. The loading ratio was calculated according to the following equation. Subsequently, it was washed, and vacuum freeze-dried to obtain DMUP powder.

$$\text{Loading ratio } (\%) = (\text{weight of Pae in DMUP/ weight of DMUP}) \times 100\% \quad (1)$$

Effect on macrophage polarization

Mouse monocyte macrophage leukemia (RAW264.7) cells were inoculated on cell slides in six-well plates at a density of 1×10^6 cells per well and warmed at 37 ℃ for 24 h. Cells were pretreated with 200 μg mL^{-1} of different samples for 24 h, treated with 10 μg mL^{-1} lipopolysaccharide (LPS) for 12 h, and then washed three times with phosphate-buffered saline (PBS). Subsequently, cells were fixed with 4% paraformaldehyde for 15 min, washed several times with PBS, and closed with 3% bovine serum albumin (BSA) for 30 min. CD86 (1:100 dilution) and CD206 (1:200 dilution) primary antibodies were co-cultured with cells at 4 ℃ overnight, and washed with PBS. Next, samples were incubated with Cy3-labeled goat anti-rabbit IgG antibody (1:300 dilution) for 1 h. After three times of washing, the nuclei were stained with 4′,6-diamidino-2-phenylindole (DAPI). Finally, cells were observed using a fluorescence microscope (ECLIPSE C1, Nikon, Japan).

Hemolysis test

To obtain erythrocytes, fresh blood from rats was centrifuged at 1500 rpm for 15 min, washed gently, and diluted with saline. Then, 100 μL of erythrocyte solution was mixed with 1.1 mL of different concentrations of DMUP solution (25, 50, 100, 200, 400 μg mL^{-1}). Meanwhile, 100 μL of erythrocyte solution was mixed with 1.1 mL of physiological saline and deionized water, which were used as negative and positive controls, respectively. After incubation at 37 ℃ for 3 h, the supernatants of all groups were collected by centrifugation at 1500 rpm for 15 min. The absorbance at 540 nm of each sample was determined by a microplate reader. The hemolysis rate was calculated according to the following formula:

$$\text{Hemolysis ratio } (\%) = (OD_e - OD_p) / (OD_w - OD_p) \times 100\% \quad (2)$$

Intracellular ROS scavenging activity

Bacterial-derived LPS was selected for inducing endogenous oxidative stress in RAW264.7 cells. To induce endogenous oxidative stress, RAW264.7 cells were inoculated in 24-well plates at a density of 5×10^5 cells per well and incubated for 24 h. Then, 100 μL of 10 μg mL^{-1} LPS containing Dulbecco's modified eagle culture medium (DMEM) and different concentrations of samples were co-cultured for 12 h. The medium was then replaced with 2,7-dichlorodihydrofluorescein diacetate (DCFH-DA), which could be oxidized to 2,7-dichlorofluorescein (DCF) by ROS, and then co-cultured with the cells for 30 min. The cells were observed with an inverted fluorescence microscope, and the fluorescence quantification of DCF was measured by fluorescence analysis (Ex: 488 nm, Em: 525 nm).

In vivo imaging experiments

All animal experimental protocols were approved by the Animal Ethics Committee of Nanchang University, China (NCULAE-20221228041). Eighteen male Sprague Dawley (SD) rats (8 weeks old, 150–200 g) were randomly divided into 7 groups ($n = 6$). 500μL suspension of physiological saline with various concentrations (0, 10^4,

10^5, 10^6, 10^7, 10^8, 10^9CFU mL^{-1}) of mixed *P. gingivalis*, *Escherichia coli* (*E. coli*), and *Staphylococcus aureus* (*S. aureus*) was injected into the bilateral hind leg muscles of the rats. After three days, infected rats with muscle infections were obtained for the experimental groups. Moreover, the infected muscles of the right side of the rats were sampled. H&E staining was conducted to observe the cell morphology of the muscle tissues and to verify the successful establishment of the infection model. Subsequently, NIR-II small animal imaging was performed 10 min after the injection of 500 µL DMUP at the synchronized site (groups of 0, 10^6, 10^7, 10^8, and 10^9CFU mL^{-1}) to observe the DMUP-labeled fluorescence imaging area images.

Modeling and treatment of experimental periodontitis

To evaluate the combined therapeutic efficacy of DMUP in periodontitis, we established a typical bacterial-induced periodontitis model in rats. After 1 week of acclimatization, 24 male SD rats (8 weeks old, 150–200 g) were randomly divided into 4 groups ($n = 6$): no treatment group (Sham), periodontitis + PBS (Con), periodontitis + MC, and periodontitis + DMUP. 3–0 silk threads were used to ligate the left maxillary second molars of rats, while daily injections of a mixed bacterial solution of *P. gingivalis*, *S. aureus*, and *E. coli* mixture (10^9 CFU mL^{-1}, 500 µL), and high-sugar drinking water (100 g L^{-1} glucose). After a total of 14 days, 100 µL of PBS, MC, DMU, and DMUP (200 µg mL^{-1}) was injected into periodontal pockets every alternate day. Four weeks later, maxillae with teeth harvested from the executed rats were collected for micro-computed tomography (Micro-CT) analysis, H&E staining, immunohistochemical staining, and Masson staining. Samples were scanned by Micro-CT (NEMO NMC-200, PINGSeng Healthcare Inc.). The vertical distance between the ABC and CEJ as well as the bone volume per tissue volume (BV/TV), and trabecular thickness (Tb. Th) were measured by three-dimensional reconstruction (AVATAR 1.7.0, PINGSeng Healthcare Inc.).

Statistical analysis

All quantitative data are expressed as mean ± s.d. Data processing and statistical analysis were performed using GraphPad Prism 9.5.0. All experiments were repeated at least three times. Data were analyzed using a t-test and one-way analysis of variance (ANOVA). Data are expressed as means ± s.d. ($n \geq 3$), with $^{*}p < 0.05$, $^{**}p < 0.01$, $^{***}p < 0.001$, and $^{****}p < 0.0001$ denoting significance.

Results and discussion

Synthesis and characterization of DMUP

Figure 2a illustrates the synthesis process of the NIR-IIb fluorescence imaging multifunctional nanozyme platform (DMUP). First, a thermal decomposition method was utilized to synthesize 980 nm NIR-responsive DCNPs with a core-shell structure (Fig. 2b and c, and S1) [38]. The resulting DCNPs were homogeneous monodispersed hexagonal core-shell nanoparticles with a particle size of about 35 nm. To increase the hydrophilicity and facilitate the subsequent functional steps, a layer of $mSiO_2$ approximately 30 nm thick was grown on the surface of the DCNPs, resulting in DCMS (Fig. 2d and S2). Subsequently, the DCMS surface was functionalized to form DCMS-COSR. Then, Mn nanozyme was precipitated into the pores of DCMS-COSR, followed by the grafting of UBI_{29-41} onto its surface and the loading of Pae into remaining pores, ultimately forming the resultant complex called DMUP. As shown in Fig. 1, the transmission electron microscopy (TEM) image revealed that the Mn nanozyme nanoparticles appeared on the surface of the DCMS in a characteristic ribbon-like structure [27, 30]. Moreover, the scanning electron microscopy (SEM) results showed a raised shape at the pores (Fig. S3). The successful preparation of DMUP was also proved by the elemental mapping results (Fig. 2f).

The grafting on the $mSiO_2$ surface began with modifying the N-terminus of UBI_{29-41} with cysteine (Fig. S4). Then, the DCMS-Mn (denoted as DM) surface reacted *via* thioesterification to form DM-COSR (Fig. S5) [39]. Finally, as shown in Figure S6, the peptide was covalently attached *via* native chemical ligation (NCL) to form DCNP@$mSiO_2$-Mn-UBI_{29-41} (denoted as DMU) [35]. We also complemented the covalent docking simulations, with Fig. S7 showing that the thiol and amine groups of cysteine in UBI_{29-41} could form covalent bonds with the carbonyl group of DM-COSR, resulting in a stable amide bond with a docking score of −9.226 kcal/mol (a docking score below −5 kcal/mol indicates bond stability). The successful synthesis of DMU was confirmed by comparing the changes in zeta potential and pH during the grafting process (Fig. 2g and S8). Fig. 2h shows the X-ray diffraction (XRD) pattern of the system. The diffraction peaks could be attributed to the hexagonal phase crystalline form of β-$NaYF_4$ (JCPDS No. 00-016-0334). Additionally, as for the $mSiO_2$ of DCMS, a broad absorption band of amorphous SiO_2 could be observed at $2\theta = 22°$. In addition, the results of Fig. 2h showed characteristic peaks consistent with the ZIF-8 crystal phase (JCPDS No. 00-062-1030), and matched with diffraction peaks of MnO_2 (JCPDS No. 00-072-1982). This supported the formation of metal-organic frameworks in DMUP pores and the hypothesis that MnO_2 served as the nanozyme's active component. And ZIF-8 metal-organic framework contributed to acid-responsive functionality. The ultraviolet-visible spectroscopy (UV-vis) spectrum of DM-COSR revealed the characteristic broad absorption peak after Mn nanozyme precipitation (Fig. S5). Moreover, the

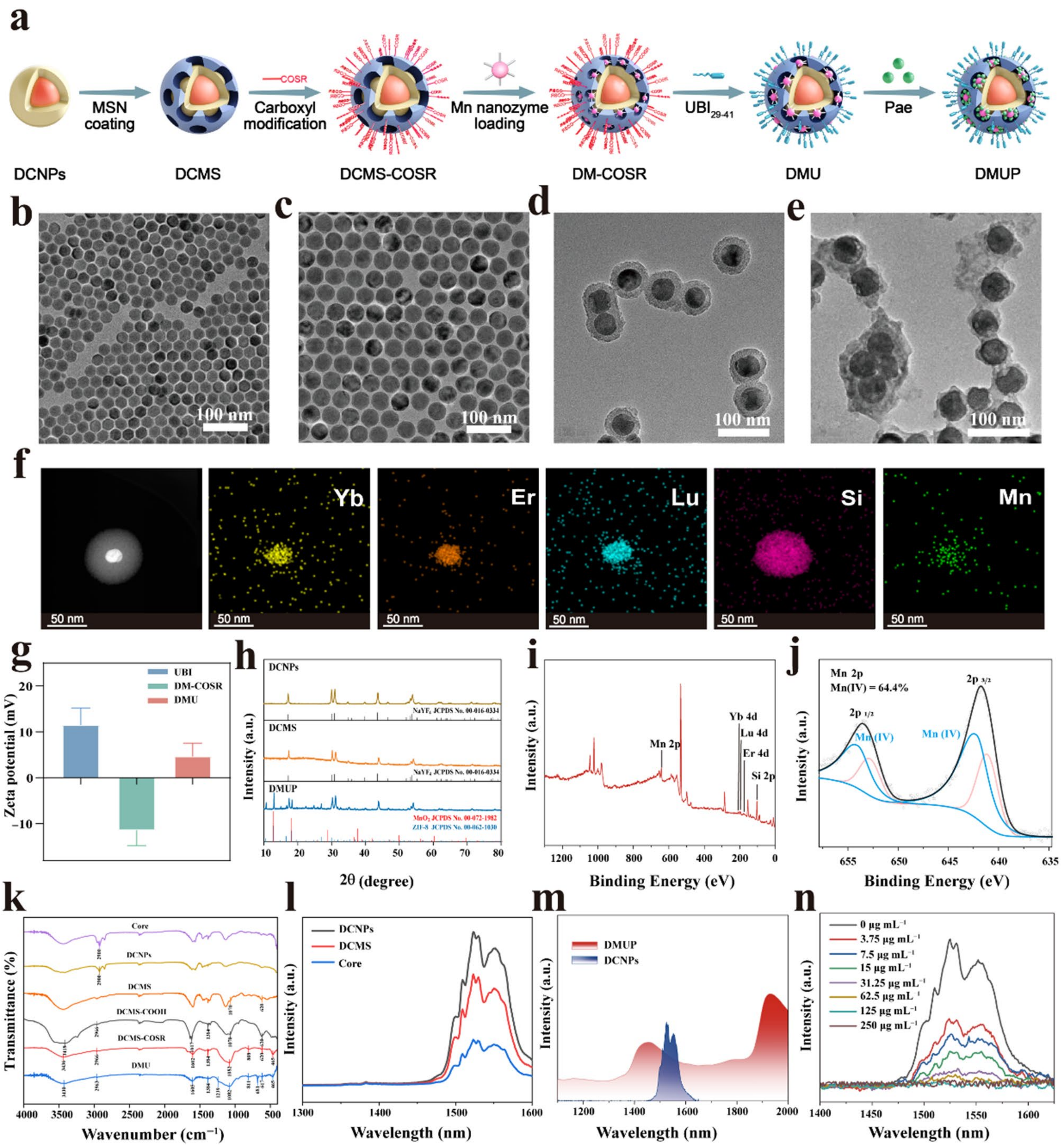

Fig. 2 Synthesis and characterization of DMUP. (**a**) A schematic diagram showing the synthesis of DMUP. The TEM images of (**b**) DCNPs core, (**c**) DCNPs, (**d**) DCMS, and (**e**) DMUP. (**f**) Elemental mapping analysis of DMUP. (**g**) Zeta potential changes of the DM-COSR before and after being surface grafted of UBI_{29-41}. (**h**) XRD patterns of DCNPs, DCMS, and DMUP. (**i**) XPS energy spectrum for DMUP. (**j**) The fitted peak spectrum of the Mn element after deconvolution. (**k**) FTIR spectra of Core, DCNPs, DCMS, DCMS-COOH, DCMS-COSR, and DMU. (**l**) NIR-IIb fluorescence broad spectra of the DCNPs core, DCNPs and DCMS. (**m**) NIR-IIb fluorescence spectrum of DCNPs under 980 nm excitation and NIR-IIb absorption spectrum of DMUP. (**n**) Fluorescence spectra of DMUP synthesized with different concentrations of Mn doping in the NIR-IIb band. Data are means ± s.d. ($n \geq 3$)

X-ray photoelectron spectroscopy (XPS) fitting results revealed the Mn(IV) oxidation state in the DMUP (Fig. 2i and j). It was shown that the successful precipitation of Mn nanozyme nanoparticles demonstrated the potential performance of tetravalent manganese antioxidant nanozyme [40]. Meanwhile, fourier transform infrared (FTIR) was utilized to detect the functional groups (Fig. 2k). The FTIR spectra revealed C–C and C–H peaks at

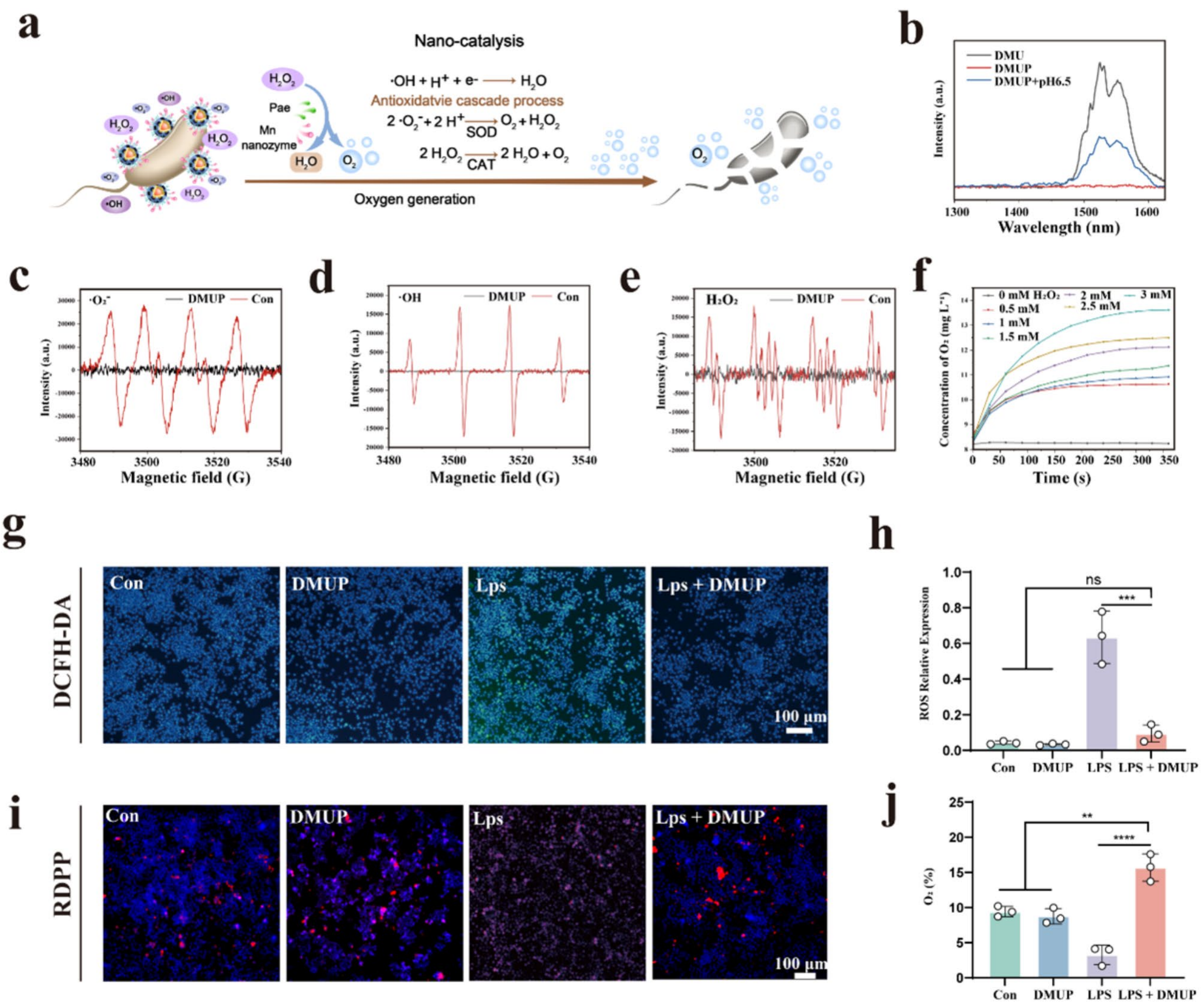

Fig. 3 Physicochemical properties and biosafety of DMUP. (**a**) Antioxidant and O_2-producing antimicrobial principle of DMUP. (**b**) NIR-II fluorescence spectra of DMU, DMUP, and DMUP (pH = 6.5). (**c – e**) ESR spectra of scavenging of $\cdot O_2^-$, ·OH, and H_2O_2 by DMUP. (**f**) Analysis of the O_2 yield as a result of the interaction of DMUP with different concentrations of H_2O_2. (**g**) Representative fluorescence microscopy images of DMUP on intracellular ROS. Blue: nucleus of cell, Green: intracellular ROS. (**h**) Relative fluorescence quantification results of intracellular ROS by DMUP. (**i**) Images of fluorescence microscopy detection intracellular O_2. Blue: nucleus of cell, Red: hypoxia in cells. (**j**) Results of O_2 content occupancy analysis. Data are means ± s.d. ($n \geq 3$), ns: no significant difference, $^{**}p < 0.01$, $^{***}p < 0.001$, $^{****}p < 0.0001$

2900 cm^{-1}, which were characteristic of the DCNPs [38]. The C = O stretching vibration peaks between 1700 and 1725 cm^{-1}, and the enhancement of the O – H bonds between 2500 and 3300 cm^{-1}, demonstrated the successful modification of the – COOH (DCMS-COOH). Moreover, the characteristic peaks of the aryl ring at 750–800 cm^{-1} indicated the success of thioesterification (DCMS-COSR) [39].

The fluorescence properties during the synthesis of DMUP were characterized as shown in Fig. 2l. DCMS exhibited a strong emission peak in the 1500–1600 nm NIR-IIb fluorescence band under 980 nm excitation. The broad absorption of Mn nanozyme in the NIR band (Fig. 2m) led to FRET action along with the precipitation of Mn nanozyme in the pore. As shown in Fig. 2n, the NIR-IIb fluorescence of DMUP was gradually quenched. The final effectively quenched $KMnO_4$ synthesized concentration was estimated to be 62.5 μg mL^{-1}. The successful loading of Pae was illustrated in Fig. S9 and S10. The XPS spectrum and inductively coupled plasma-mass spectrometry (ICP-MS) results of DMUP revealed the presence of Er, Yb, Lu, and Si elements in DMUP, further confirming the successful loading of each component in DMUP (Fig. S11–S15).

Assessment of physicochemical properties and biosafety of DMUP

ROS are byproducts of normal metabolism, typically neutralized by the antioxidant system of body under normal physiological conditions. During the progression of periodontitis, the immune system becomes hyperactive due to the increase in anaerobic pathogenic bacteria. This process increases the amount of ROS in the periodontal tissues, which causes an imbalance between ROS and the antioxidant system, resulting in a toxic response, thereby exacerbating periodontitis [41]. Meanwhile, with the accumulation of plaque, the periodontal microenvironment shifts from a normoxic to a hypoxic phase. The resultant deep hypoxic environment further exacerbates the colonization of pathogenic anaerobic bacteria [42, 43]. Therefore, in order to modulate the changes in the periodontitis microenvironment, this study verified the acid response, antioxidant system release, CAT-like, SOD-like, and catalytic antioxidant nano-enzymatic properties of DMUP.

Figure 2a shows the involvement of reactive oxygen species in cellular respiration. First, O_2 gained an electron to form $\cdot O_2^-$, which was then converted to H_2O_2 by SOD. Next, CAT decomposed H_2O_2 to H_2O and O_2 [28]. During the anti-inflammation process, the excess ROS is scavenged to produce O_2, which alleviates the hypoxic environment and inhibits the anaerobic bacteria [26]. The ICP-MS and UV-vis spectroscopy (Fig. S16 and S17) results revealed that Mn oxides and Pae release increased under acidic conditions, providing the basis for a cascade catalytic reaction to excess ROS. Then, Fig. 2b demonstrated that DMUP could recover NIR-II fluorescence in acidic conditions due to the removal of Mn oxides from the pores, which eliminated FRET effects [30]. Electron spin resonance (ESR) was utilized to confirm that DMUP exhibited CAT-like and SOD-like activities by scavenging $\cdot OH$, $\cdot O_2^-$ and H_2O_2. Figure 2c–e showed that DMUP scavenges significant amounts of $\cdot OH$, $\cdot O_2^-$ and H_2O_2. Additionally, this study also addressed the issue of hypoxia in periodontal pockets. The H_2O_2 produced by the hyperactive immune response in inflamed tissues and the periodontal pocket bacterial biofilm during metabolism aggravates tissue damage [44]. Mn nanozyme incorporation provided DMUP with a strong ability to decompose H_2O_2 into O_2 (Fig. S18), which was extremely significant in the treatment of periodontal diseases. Adequate O_2 production effectively alleviated periodontal pocket hypoxia, improved the hypoxic environment [26], and inhibited the proliferation of anaerobic pathogenic bacteria. As shown in Fig. 2f, DMUP could catalyze O_2 production in different concentrations of H_2O_2 solution.

Encouraged by the excellent ROS scavenging and catalytic H_2O_2 O_2-producing ability of DMUP in vitro, we next tested these properties in cells. First, the effect of DMUP on the proliferation of the macrophage RAW264.7 cells, an important immune line of defense, was evaluated. As shown in Fig. S19-S22, the results of cell counting kit-8 (CCK-8), cell live/dead staining, and hemolysis test indicated that DMUP at a concentration of 200 μg mL^{-1} was considered safe and used in subsequent cell experiments. Subsequently, bacterial LPS was selected to induce an inflammatory model of endogenous oxidative stress in RAW264.7 cells [34]. The ROS probe DCFH-DA was utilized to determine the antioxidant effect of DMUP. Compared with the control (Con) group, the LPS group significantly promoted ROS production with strong fluorescence (Fig. 2g and h). In contrast, there was a fluorescence quenching in the DMUP group, indicating a reduction in the intracellular ROS level. This clearly suggested that DMUP reduced endogenous oxidative stress. Next, the intracellular O_2 production capacity of DMUP in RAW264.7 was investigated by tris (4,7-diphenyl-1,10-phenanthroline) ruthenium (II) dichloride ($[Ru(dpp)_3]Cl_2$), a luminescent probe commonly used for O_2 identification and quantification (Fig. 2i and j). In contrast to the Con group, the amplification of red luminescence indicated a decrease in the O_2 content of the LPS-induced inflammatory cells. After incubating with DMUP for 2 h, the attenuation of red luminescence confirmed O_2 production (Fig. S23). This result demonstrated that DMUP had a good intracellular ability to catalyze O_2 production. Therefore, the catalytic decomposition of ROS could reduce inflammation by regulating the redox imbalance and hypoxic state at the inflammatory site.

Validation of DMUP targeted bacteria and imaging capabilities

UBI_{29-41} targets bacterial surfaces by electrostatically adsorbing to phosphatidylglycerol and attracting hydrophobic bacterial membranes. Therefore, UBI_{29-41} could be specifically targeted to the bacterial surface by DMUP through surface grafting, which was also the basis for accurate bacterial imaging (Fig. 4a). SEM was used to study the interaction between DMUP and *P. gingivalis*, *E. coli*, and *S. aureus* after 30 min of incubation at pH 6.5 (Fig. 4b – d). The corresponding images revealed that DMUP was able to target and adhere to the surface of all three bacteria. The targeting efficacy of DMUP was evaluated by loading fluorescein isothiocyanate (FITC, denoted as DMUP-F) into DMUP. DMUP-F was co-cultured with *P. gingivalis* for 5, 10, 20, and 30 min and observed under a fluorescence microscope (Fig. S24a). Combined with the results of the quantitative fluorescence analysis (Fig. S24b), it was confirmed that DMUP effectively targeted bacteria after co-cultivation for 10 min.

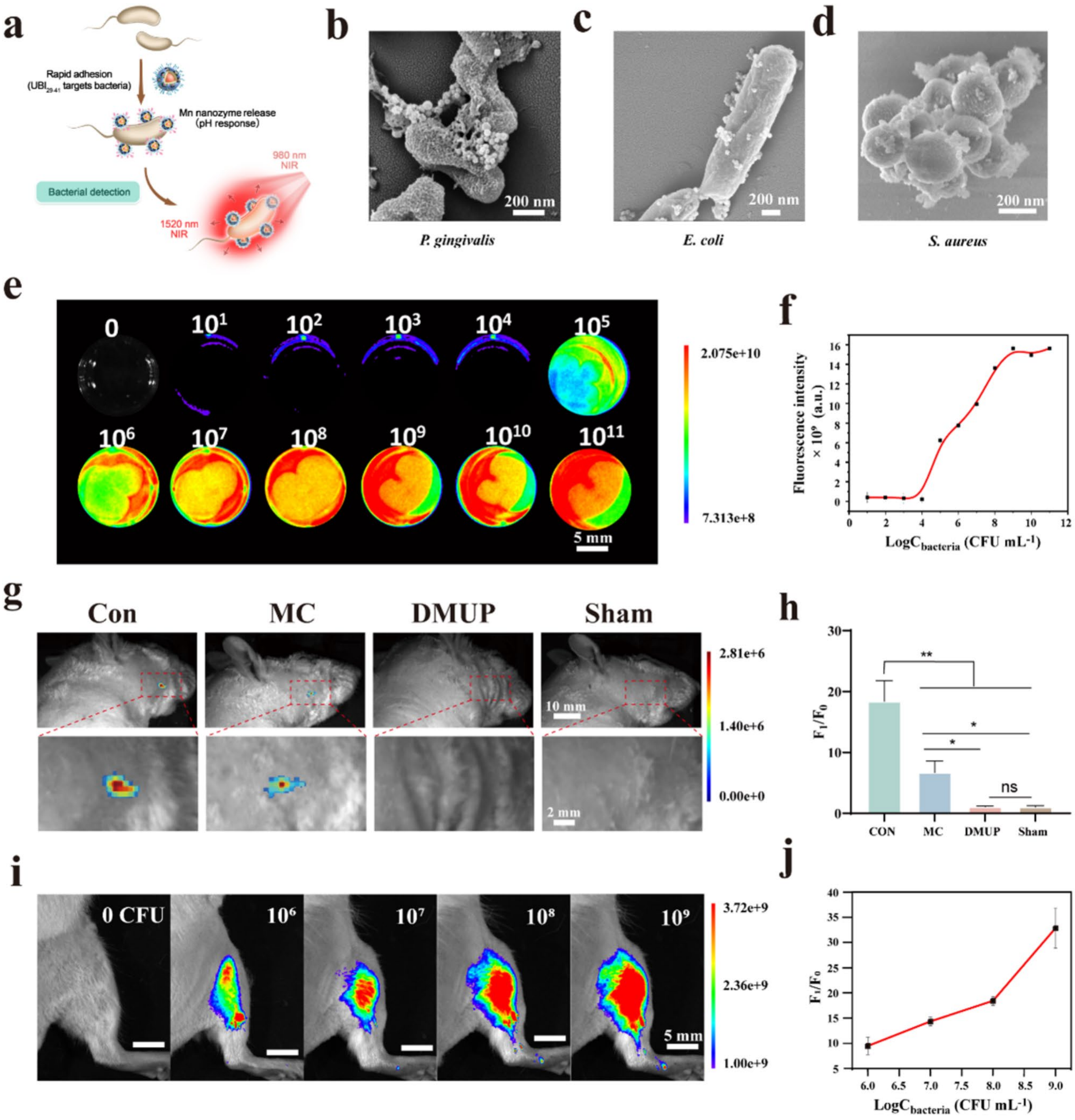

Fig. 4 Imaging capabilities of DMUP-targeted bacteria. (**a**) Schematic of DMUP-targeted bacteria and acid-responsive fluorescence imaging. Representative SEM images of DMUP targeting (**b**) *P. gingivalis*, (**c**) *E. coli*, and (**d**) *S. aureus*. (**e**) NIR-II fluorescence images of DMUP on different concentrations of mixed bacteria, and (**f**) quantification results of fluorescence intensity. (**g**) NIR-II images of infected areas of periodontitis in rats, and (**h**) the results of fluorescence relative intensity. (**i**) NIR-II images of the bacterial infection model in the leg, and (**j**) the results of fluorescence relative intensity. Data are means ± s.d. ($n \geq 3$), ns: no significant difference, $^{*}p < 0.05$, $^{**}p < 0.01$

The DMUP (200 μg $\mathrm{mL^{-1}}$) was evaluated for imaging *P. gingivalis*, *E. coli*, and *S. aureus*. As shown in Fig. 4e, all three bacteria were mixed in equal proportions, grouped in different concentrations, and incubated with DMUP for 10 min. A NIR-II small animal imager was used to detect the fluorescence intensity of each group. The bacterial concentration positively correlated with the fluorescence intensity in the 10^4–10^9 CFU $\mathrm{mL^{-1}}$ bacterial concentration group (Fig. 4f). In contrast, the fluorescence intensity of the 10^1–10^4 CFU $\mathrm{mL^{-1}}$ bacterial concentration group was too weak to be recorded. Moreover, there was no significant difference in the fluorescence intensity in the 10^9–10^{11} CFU mL^{-1} bacterial concentration group. This lack of difference was likely due to the limited acidity of the environment around the bacteria, which did not decrease indefinitely with the increased bacterial concentration [45]. Therefore, the findings of the experiments indicated that the effective bacterial detection concentration was 10^4 CFU mL^{-1} or more when using a DMUP concentration of 200 μg mL^{-1}.

The classical model of bacteria-induced periodontitis in rats was used to evaluate the effect of DMUP for imaging bacteria in periodontal pockets (Fig. 4g and h). The results showed that DMUP still had the ability to image bacteria in the rugged structure of the periodontal pockets. The Con group had the highest fluorescence intensity, while the DMUP group had the lowest. Then, comparative bacterial plating experiments were conducted on the periodontal pockets of different groups to evaluate bacterial load differences. Figure S25 showed that the DMUP group exhibited the strongest antibacterial effect, consistent with the intensity of fluorescence in the corresponding group. These results supported DMUP's targeting and imaging capabilities in periodontal infection sites. However, the periodontal pockets of rats were too small, making it difficult to observe bacterial concentration-dependent changes in fluorescence intensity. To better simulate larger-scale in vivo imaging, we selected an SD rat leg muscle infection model. This model exhibits strong similarities to periodontal tissue infections, such as excess ROS, hypoxic conditions, and the coexistence of anaerobic and aerobic bacteria [46]. The bacteria displayed prominent proliferation when injected at 10^6 CFU mL^{-1} in the rat (Fig. S26). Furthermore, the muscle fibers were infiltrated with many inflammatory cells (Fig. S27), indicating that injecting 1 mL bacteria (10^6 CFU mL^{-1}) or more could successfully create a model leg muscle infection. To further verify the performance of in vivo bacterial imaging, as illustrated in Fig. 4i, different concentrations of mixed bacteria were imaged in the leg muscle after injecting 500 μL DMUP (200 μg mL^{-1}). The imaging results of small animals, analyzed by the fluorescence intensity ratio, showed a positive correlation with the injected bacterial concentrations, indicating that DMUP could effectively image the bacteria within the inflammation (Fig. 4j).

Study of antimicrobial and anti-biofilm activity of DMUP

Bacteria and plaque as initiators of periodontitis. The antimicrobial activity of DMUP was examined on the following bacteria: *P. gingivalis* (typical pathogenic anaerobic bacteria), *S. aureus* (typical aerobic bacteria), and *E. coli* (typical facultative anaerobic bacteria). First, exogenous H_2O_2 (1 mM) was added to the medium and the pH was adjusted to 6.5. A titrimetric method was utilized to examine the antimicrobial activity of different concentrations of DMUP against 10^5 CFU mL^{-1} of *P. gingivalis*, *E. coli*, and *S. aureus*. The results revealed that the minimal inhibitory concentrations of DMUP against *P. gingivalis* and *E. coli* were 200 μg mL^{-1} and 1600 μg mL^{-1}, respectively (Fig. S28). In contrast, the antimicrobial efficiency against the aerobic *S. aureus* was lower, with no significant bacterial inhibition at 1600 μg mL^{-1}, which was in keeping with the antimicrobial needs of periodontitis. Since the main causative organisms of periodontitis are anaerobes, treatment focuses on anti-anaerobes. Therefore, in conjunction with the biosafety concentration, we chose the lowest antimicrobial concentration of DMUP (200 μg mL^{-1}) against the anaerobic bacterium *P. gingivalis* for subsequent experiments.

SEM was used to observe the different degrees of cell membrane rupture and contraction of *P. gingivalis*, *E. coli*, and *S. aureus* by 200 μg mL^{-1} of DMUP (Fig. 5a). As shown in Fig. 5b, the spread plate method revealed antimicrobial rates of about 99.9%, 95.7%, and 63.5%. This indicated that DMUP exhibited varying antimicrobial activities against the three bacteria. Particularly, the inhibition of the anaerobic bacteria by DMUP was superior to that shown by a conventional drug and the MC group. Moreover, since plaque biofilm was considered to be the initiating factor of periodontitis, the efficiency of DMUP for removing *P. gingivalis* biofilm was examined by live/dead staining (Fig. S29 and S30) and crystal violet (CV) staining experiments. As shown in Fig. 5c and d, the results revealed that with a removal rate of about 96%, DMUP exhibited the best removal efficiency against *P. gingivalis* biofilm. Against *E. coli* and *S. aureus*, the removal rates were about 81%, and 27%, respectively. Thus, this indicated that DMUP exhibited superior performance in removing anaerobic bacterial biofilm.

This study also elucidated the antibacterial mechanism of DMUP. The destruction of bacterial cell membranes in a biofilm was investigated with a protein leakage assay. The results revealed that protein leakage was consistent with those of the anti-biofilm experiments (Fig. S31–S33). Subsequently, the expression changes in genes related to *P. gingivalis*, including fimbrial protein A (fimA), keratinsulfate glycoprotein (kgp), arginine-specific gingipain A (rgpA), and arginine-specific gingipain B (rgpB), were detected after treatment. The analysis revealed that DMUP effectively reduced the expression levels of the above genes (Fig. 5e–h). Thus, the findings suggested that DMUP destroyed the cell membranes of anaerobic bacteria by inhibiting the expression of the virulent genes of *P. gingivalis*. With an antibacterial efficiency higher than that of conventional drug MC, DMUP exhibited an excellent anti-biofilm effect against anaerobic bacteria. However, its antibacterial performance against aerobic bacteria was limited. As periodontitis progresses, anaerobic bacteria primarily contribute to tissue destruction

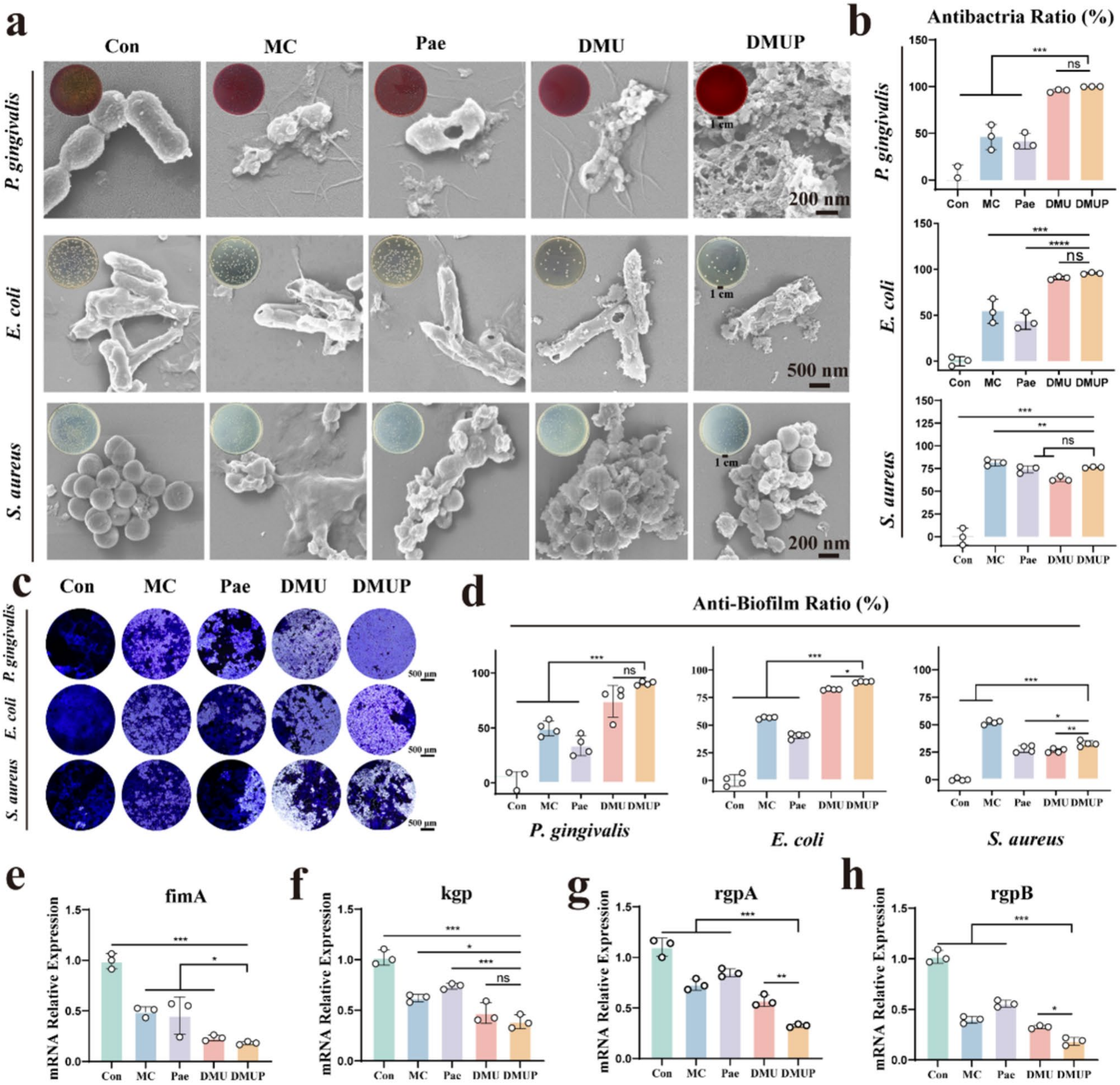

Fig. 5 Antibacterial and anti-biofilm activity of DMUP. (**a**) Representative plate images and SEM images after co-incubation of DMUP with *P. gingivalis*, *E. coli*, and *S. aureus*, respectively. (**b**) Results of antimicrobial properties after quantification. (**c**) Representative light microscopic pictures of CV staining of three biofilms. (**d**) Anti-biofilm rates of different groups for the three biofilms. (**e**–**h**) Changes in the expression of *P. gingivalis* virulence genes after treatment in different groups. Data are means ± s.d. ($n \geq 3$), ns: no significant difference, $^{*}p < 0.05$, $^{**}p < 0.01$, $^{***}p < 0.001$, $^{****}p < 0.0001$

[47]. Thus, the superior performance of DMUP in inhibiting anaerobic bacteria was in line with the requirements for periodontitis treatment.

Experimental studies of anti-inflammatory in vitro

Several signaling pathways, such as NF-κB and MAPK, are activated by excess ROS generated by an inflammatory response, which promotes the expression of inflammatory factors [48, 49]. ROS clearance can block intracellular signaling functions and damage cellular structures, alleviating symptoms and retarding disease progression [50, 51]. Thus, an important component of the treatment of inflammatory and immune diseases involves controlling ROS levels and reducing the expression of inflammatory factors. In this study, the activated inflammation was modeled with the mouse macrophage cell line RAW264.7 cells. The anti-inflammatory capacity of DMUP in vitro was determined by examining the gene expression of key pro-inflammatory and anti-inflammatory mediators in the inflammatory process after inducing inflammation in the RAW264.7 cells (Fig. 6a). In the quantitative real-time polymerase chain reaction (qRT-PCR) results, the gene expression of pro-inflammatory factors tumor necrosis factor-α (TNF-α), transforming growth factor-β (IL-1β), and interleukin-6 (IL-6) increased significantly in LPS-treated RAW264.7 cells, while the gene expression of anti-inflammatory factor transforming growth factor-β (TGF-β) decreased relatively (Fig. 6b and c and S34). After DMUP (200 μg mL^{-1}) treatment, there was a significant decrease in the expression of TNF-α, IL-1β, and IL-6. In contrast, expression of the anti-inflammatory factor TGF-β was elevated. Furthermore, the expressions of TNF-α and IL-6 were significantly reduced in the DMU group. In contrast, the expression of IL-1β was not statistically different from that of the LPS group. The gene expression of TNF-α and IL-1β was significantly more reduced in the Pae group than that in the DMU group. However, the reduction in the expression of IL-6 was lower in the Pae group than that in the DMU group. The changes in the expression of the three pro-inflammatory factors revealed that the DMUP group displayed the strongest ability to reduce them. Although there were differences between the Pae and DMU groups in the expression of the pro-inflammatory factor TGF-β, DMUP had the most pronounced effect on its elevation. This might be attributed to the synergistic anti-inflammatory effect of Mn nanozyme and polyphenolic antioxidants in the DMUP system.

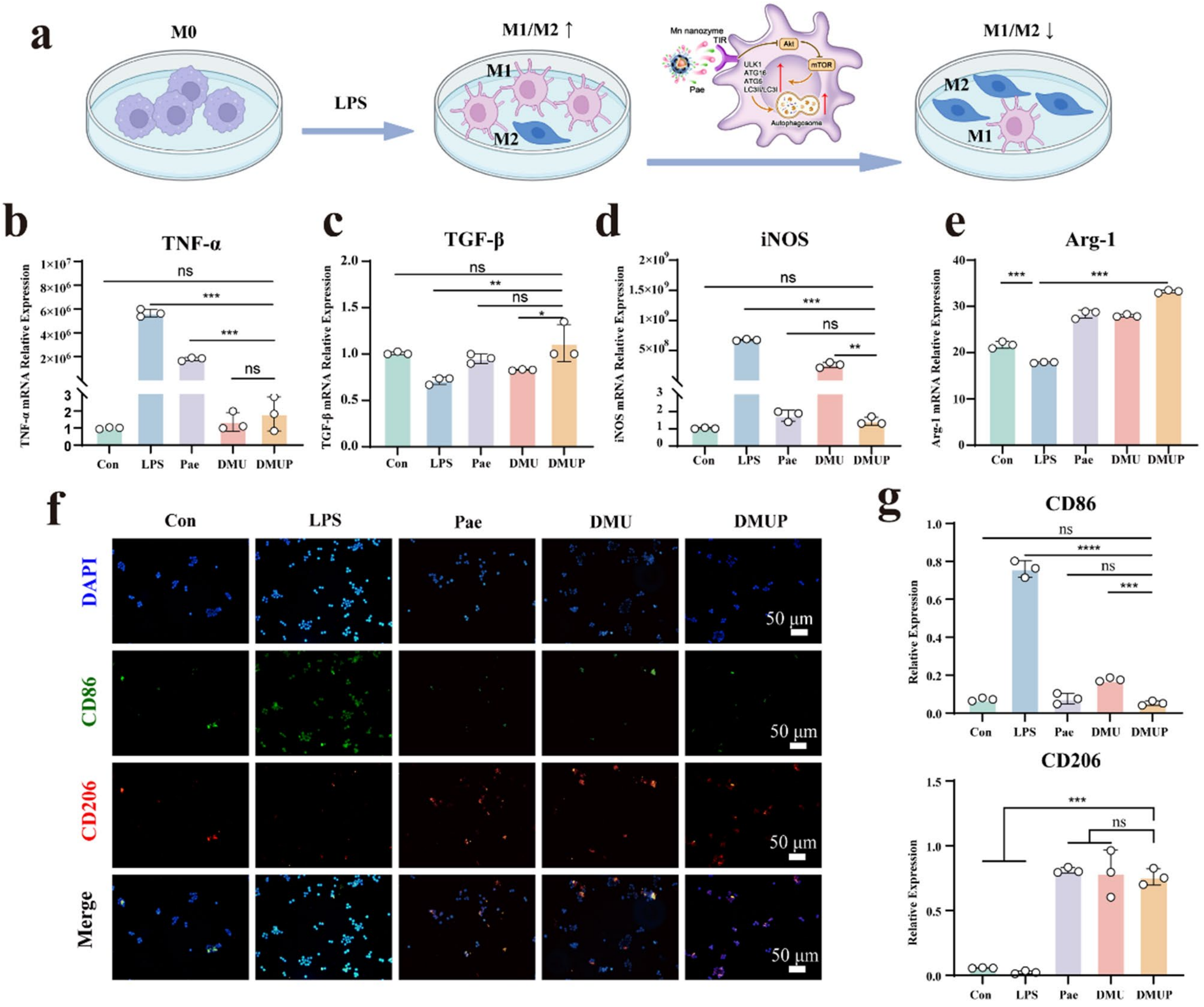

Fig. 6 In vitro anti-inflammatory efficacy evaluation of DMUP. (**a**) Schematic representation of induced inflammation RAW264.7 cells, as well as anti-inflammatory and induced autophagy. Created with BioRender. com. Gene expression of (**b**) pro-inflammatory factor TNF-α and (**c**) anti-inflammatory factor TGF-β after group treatment. (**d**) Expression of Arg-1, a representative gene of cellular anti-inflammatory phenotype M2, and (**e**) expression of iNOS, a representative gene of pro-inflammatory phenotype M1. (**f**) Representative fluorescence images of different treatment groups. (**g**) Quantitative fluorescence images of M1 (CD86), and M2 (CD206) phenotypes of RAW264.7 cells. Data are means ± s.d. ($n \geq 3$), ns: no significant difference, $^{*}p < 0.05$, $^{**}p < 0.01$, $^{***}p < 0.001$, $^{****}p < 0.0001$

The effect of DMUP on the immune function of RAW264.7 cells was examined by performing qRT-PCR assays to detect the M1-type and M2-type markers inducible nitric oxide synthase (iNOS) and arginase 1 (Arg-1) (Fig. 6d and e). Additionally, immunofluorescence (IF) assays were performed to detect cluster of differentiation 86 (CD86) and cluster of differentiation 206 (CD206) (Fig. 6f). The results exhibited an increase in the intensity of the M1-type macrophage markers iNOS and CD86. In contrast, the intensity of the M2-type macrophage markers, Arg-1 and CD206, decreased. This led to an increase in the M1/M2 ratio, which was indicative of a pro-inflammatory profile. The expression of anti-inflammatory factors in Fig. 6b–g, showing that the Pae group (the natural antioxidant) reduced the expression of genes of M1-type inflammatory cells and promoted the production of M2-type anti-inflammatory cells, compared to the LPS group. Mn nanoenzyme mimicked CAT and SOD enzyme activities [24], effectively scavenging excess ROS in the inflammatory environment. This property of Mn nanoenzyme regulated redox balance, reduced M1 macrophage-mediated inflammation, and promoted M2 macrophage differentiation, which played an anti-inflammatory and immunomodulatory role. The DMU group (Mn nanoenzyme loaded system) showed lower expression of TNF-α, iNOS, and CD86 (M1 markers) while increasing TGF-β, Arg-1, and CD206 (M2 markers). These results indicated that Mn nanozymes also contributed to macrophage phenotype switching. The results of the DMUP group were the combined effect of Mn nanozyme and Pae. Then, the high M1/M2 ratio of LPS group was reversed when the macrophages were cultured with DMUP (Fig. 6g). The above results suggested that DMUP had anti-inflammatory properties that favored anti-inflammation and tissue repair.

Molecular mechanisms of anti-inflammation and induction of autophagy in vitro

To determine the molecular mechanisms of DMUP anti-inflammatory and autophagy, RAW264.7 cells were divided into RAW, RAW + LPS, and RAW + LPS + DMUP groups (abbreviated as Con, LPS, and DMUP) for seq-RNA and bioinformatics analysis induction in vitro. The results of the principal component (PC) analysis (Fig. S35) showed reasonable homogeneity within individual groups and differences between groups. All three sample groups met the quality control requirements. Based on the results of the volcano plot (Fig. S36), trend plot (Fig. S36), and trend heat map (Fig. 7a and S35), 89 genes were found to be significantly upregulated, and 319 genes were significantly downregulated in the DMUP group compared with the LPS group. Additionally, the results of the gene ontology (GO) analysis of these differentially expressed genes (DEGs, Fig. 7b) showed an enrichment of genes related to immune, inflammatory, and metabolic responses. The results of the kyoto encyclopedia of genes and genomes (KEGG) analysis revealed that these genes were significantly related to the PI3k-Akt, mTOR, NF-κB, and TNF signaling pathways (Fig. 7c), which further supported that DMUP played a role in immune cell autophagy and inflammation regulation.

Autophagy is an intracellular degradation process that reduces inflammatory injuries *via* the removal of potential pro-inflammatory molecules and maintains intracellular stability as well as immune homeostasis. The activation of autophagy has the potential to alleviate the expression of inflammatory factors, such as TNF-α and IL-1β. In contrast, autophagy is increased by the expression of anti-inflammatory cytokines, such as TGF-β, limiting the over-activation of inflammatory signals [52]. One of the important pathways in the regulation of autophagy is the Akt/mTOR pathway [53], which significantly affects the transition of macrophages from M1-type to M2-type *via* the regulation of autophagic activity [54]. Of these, the mechanistic target of rapamycin complex 1 (mTORC1) is a major negative regulator of autophagy, which inhibits autophagy *via* the suppression of key molecules for autophagy initiation (e.g., ULK1). Additionally, mTORC1-mediated inhibition could initiate the autophagy process, affecting the activity and functional status of macrophages. This could result in reduced production of pro-inflammatory factors, suppressing M1-type macrophage pro-inflammatory potential, promoting their transition to M2-type macrophages, facilitating the M2-type characteristics, and enhancing their tissue repair ability and anti-inflammatory cytokine production [55]. Here, the impact of DMUP on autophagic activity was confirmed *via* a number of autophagosomes and autophagic protein markers. The Monodansylcadaverine (MDC) staining results revealed that M1-type macrophages treated by DMUP possessed higher autophagosome content than untreated M1-type macrophages (Fig. S39 and S40). Next, Western blot (WB) assay was used to determine the expression of autophagic activity protein markers, autophagy initiation markers (ULK1), autophagic vesicle markers (ATG16, ATG5), and autophagy flux markers (LC3II/LC3I). The relative band intensities suggested that the levels of ULK1, ATG16, ATG5, and LC3II/LC3I were elevated in M1-type macrophages treated with DMUP (Fig. 7d and e). This implied that DMUP-activated autophagy and enhanced the autophagic flux in M1-type macrophages. Next, the signaling changes of Akt and mTOR in DMUP-treated M1-type macrophages were investigated. Initially, the Akt and mTOR signaling was active in M1-type macrophages; However, after incubation with DMUP, p-Akt and p-mTOR signaling was inactivated (Fig. S41 and S42). The above results suggested that DMUP promoted

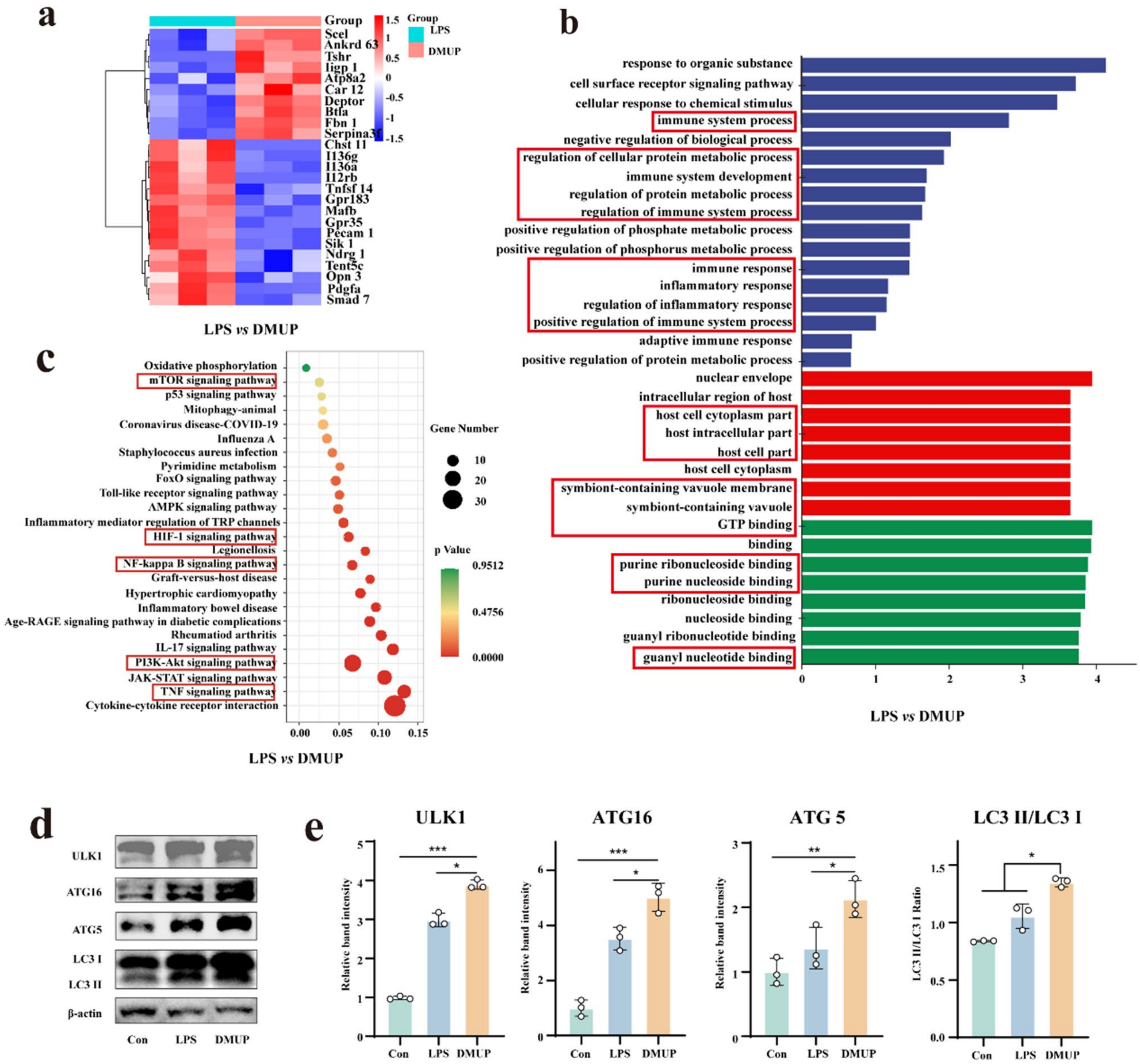

Fig. 7 To investigate the molecular mechanisms of DMUP anti-inflammation and autophagy induction at the cellular level. (**a**) Clustering heatmap of RNA-seq with gene expression results (LPS *vs* DMUP), blue: low expression; red: high expression. (**b**) GO enrichment analysis (LPS *vs* DMUP). (**c**) KEGG enrichment analysis (LPS *vs* DMUP), and related pathways pooled by differential genes. (**d**) WB assay determination of autophagy-related protein expression levels and (**e**) quantitative analysis. Data are means ± s.d. ($n \geq 3$), $^{*}p < 0.05$, $^{**}p < 0.01$, $^{***}p < 0.001$

autophagic activity *via* the inactivation of the Akt/mTOR signaling pathway to further prevent macrophage conversion to pro-inflammatory M1-type subtype, facilitating tissue anti-inflammation and repair.

Thus, the multi-enzyme system of DMUP reduced the expression of inflammatory cytokines, enhanced the autophagic flux of immune cells, and regulated both immune cell function and inflammation reduction. This, in turn, improved the tissue repair potential and anti-inflammatory cytokine production, preserving the intracellular stability and immune homeostasis and finally reducing the inflammatory injury.

Regulating the effect of the inflammatory environment on in vitro osteogenesis

During inflammation, regulation of the mechanisms involved in the alteration of macrophage polarization status, autophagy induction, decreasing ROS and pro-inflammatory factor levels, and increasing anti-inflammatory factor expression can create a microenvironment favoring osteogenesis [55]. The study also explored the role of DMUP-regulated inflammatory state macrophages in the regulation of osteogenesis in vitro.

As shown in Fig. 8a, the conditioned medium was configured. First, the induction of RAW264.7 cells by LPS

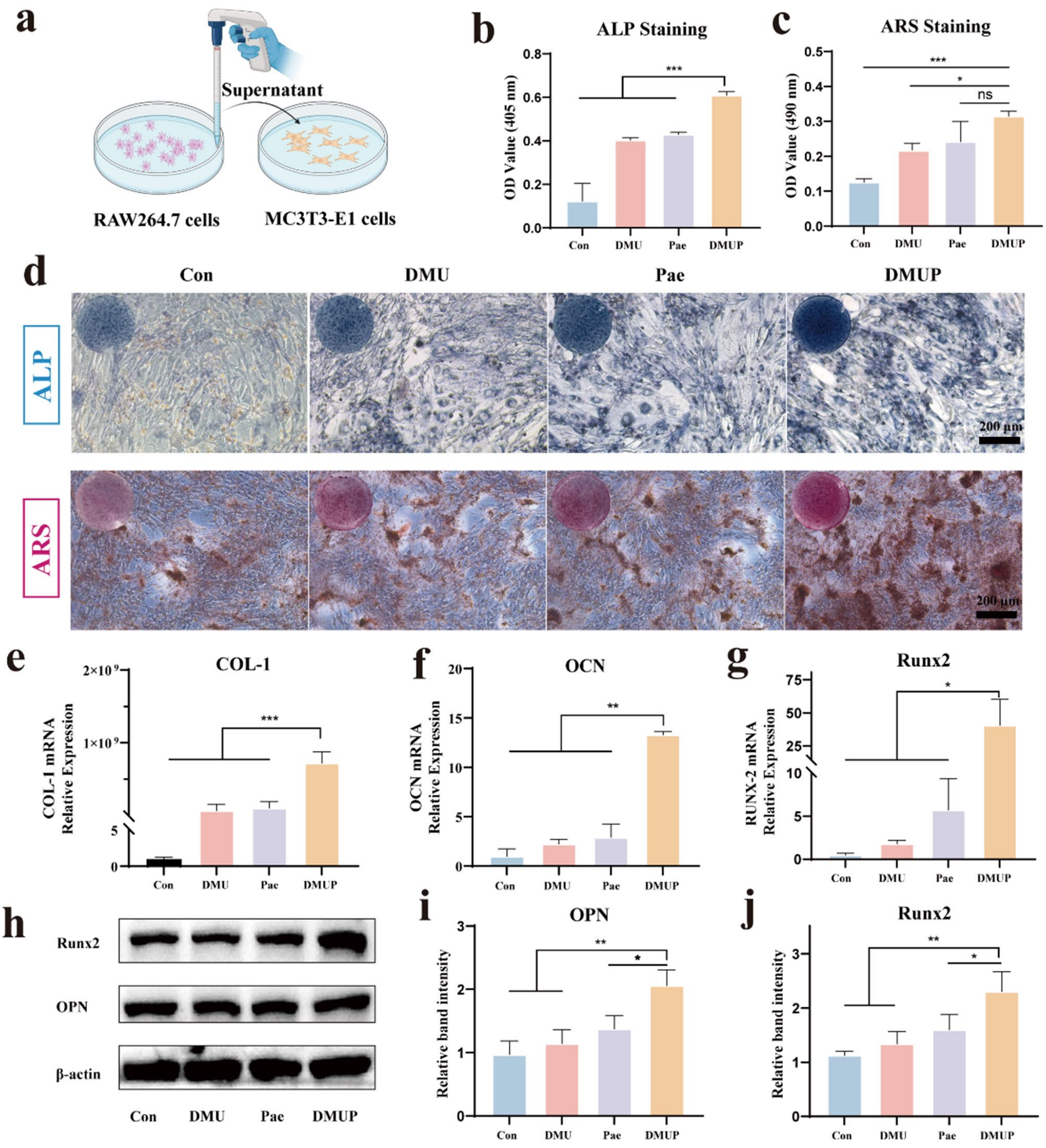

Fig. 8 Effect of DMUP on osteoblast mineralization after adjusting the inflammatory microenvironment. (**a**) Schematic of conditioned medium preparation. Created with BioRender. (**b**) Semi-quantitative results of ALP staining. (**c**) Semi-quantitative results of ARS staining of mineralized nodules, and (**d**) microscopic staining diagrams. Changes in the expression of osteogenesis-related genes (**e**) COL-1, (**f**) OCN, and (**g**) Runx2. (**h**) WB assay determination of osteogenesis-related protein expression levels, and quantification of (**i**) OPN and (**j**) Runx2. Data are means ± s.d. ($n \geq 3$), ns: no significant difference, $^{*}p < 0.05$, $^{**}p < 0.01$, $^{***}p < 0.001$

to the inflammatory state. Next, DMUP (200 μg mL^{-1}) was added and cultured for 24 h. The supernatant was used to culture the mouse embryonic osteoblast precursor (MC3T3-E1) cell [56]. The results showed that the conditioned medium, post-LPS induction (Con group), reduced the alkaline phosphatase (ALP) activity of MC3T3-E1 cells. Also, the DMUP-treated conditioned medium enhanced ALP activity of MC3T3-E1 cells (Fig. 8b). The alizarin red staining (ARS) showed similar results (Fig. 8c). Their micrographs were also significantly different (Fig. 8d). The DMUP-conditioned medium group stimulated the formation of mineralized nodules. Subsequently, the results of the qRT-PCR assay showed that DMUP upregulated the expression of osteogenesis-related genes collagen type I (COL-1), osteocalcin OCN, and runt-related transcription factor 2 (Runx2) (Fig. 8e–g).

The osteopontin (OPN) and Runx2 are two vital proteins involved in osteogenesis, which include various osteogenesis-related pathways (wnt/β-catenin, TGF-β/Smad, PI3K/Akt) and impact osteoblast differentiation, bone matrix formation, and mineralization [57]. Here, a WB assay was performed to evaluate the expression of OPN and Runx2. The DMUP-conditioned medium group exhibited elevated expression of OPN and Runx2 in MC3T3-E1 cells (Fig. 8h–j). Thus, the DMUP-conditioned inflammatory microenvironment affected osteogenic metabolism at both the gene and protein levels, enhancing mineralized nodule formation and promoting cellular osteogenic potential.

In vivo assessment of the anti-inflammatory effect of DMUP

The classic bacterial-induced periodontitis model in rats, using silk-knot and mixed bacterial fluids (*P. gingivalis*, *E. coli*, and *S. aureus*) injections, was used to evaluate the in vivo anti-inflammatory effect of DMUP (Fig. 9a) [55]. Based on the bleeding analysis by intraoral probing in rats 28 days post-treatment in different groups, the DMUP group exhibited the least amount of bleeding (Fig. S43). After injecting the bromothymol blue indicator into the periodontal pocket, the inflamed tissue appeared yellow-green (Fig. S44a and S44b). The pH testing of the supernatant from homogenized infected periodontal tissue also showed a yellow-green color (Fig. S44c and S44d). Compared to the color standard of the indicator (Fig. S44e), the pH value was approximately 6.5, confirming an acidic environment. Blood tests after DMUP treatment showed no significant changes in white blood cells (WBC), mean corpuscular hemoglobin (MCH), and platelets (PLT) levels (Fig. S45). H&E staining of main organs (Fig. S46) showed no inflammation or tissue damage in the DMUP-treated group. These results confirmed that DMUP had biosafety in vivo. Subsequently, Masson and hematoxylin-eosin (H&E) staining of periodontal tissues revealed significant inflammatory cellular infiltration and collagen loss in the Con group (Fig. 9b and S47), whereas DMUP ameliorated these abnormalities and enhanced collagen deposition. The results of the semi-quantitative analyses also showed a better effect than that of the MC group (Fig. 9c and d). Next, immunohistochemical staining was used to determine the expression of pro-inflammatory factors (IL-6, IL-1β, and TNF-α) and anti-inflammatory factors (IL-10) to further assess the in vivo anti-inflammatory effects of DMUP (Fig. 9e and S48–50). The DMUP group showed reduced expression of IL-6, IL-1β, and TNF-α and enhanced expression of IL-10, further confirming that DMUP exhibited a satisfactory anti-inflammatory effect and was stronger than that of the MC group (Fig. 9f and g and S51, S52). The results suggested that DMUP reduced the inflammatory response and promoted periodontal tissue regeneration, thus playing an effective therapeutic role in the bacterial periodontitis model.

In order to evaluate the in vivo osteogenic effect of DMUP, the therapeutic effect of DMUP was evaluated using Micro-CT and histological staining after establishing a classical bacterial-induced periodontitis model in rats. The vertical distance (attachment loss, AL) between the alveolar bone crest (ABC) and the cementoenamel junction (CEJ) was considered the therapeutic index by 3D reconstruction [58]. The Con group had the longest distance between ABC and CEJ compared with the Con group, showing significant loss of alveolar bone and successful periodontitis modeling (Fig. S53). DMUP increased the values of BV/TV, Tb. Th and bone mineral density (BMD) (Fig. 9h–j and S54) and reduced the distance between ABC and CEJ compared to the Con group. The results of H&E staining of alveolar bone volume at the heel bifurcation (Fig. S55 and S56) showed that DMUP group had the highest bone volume among the groups. Next, IF was used to study the expression of OCN and Runx2 by different groups (Fig. 9k). The red fluorescence represented the expression of OCN and Runx2, respectively, and the blue color represented the DAPI stained cell nuclei. Based on the results of the quantitative fluorescence, the DMUP group exhibited elevated expression of OCN and Runx2, which was significantly higher than that of the MC group (Fig. 9l and m). Thus, DMUP significantly regulated bone formation and bone differentiation-related factors, promoting bone formation in periodontitis. The MC group also exhibited some bone formation effects. However, those were significantly different from the DMUP group, indicating that the osteogenic effect of DMUP was better than treatment with MC.

Conclusion

In summary, we have developed a responsive NIR-IIb multifunctional nanozyme platform for treating periodontitis. This platform has bacterial imaging, anti-anaerobic, anti-inflammatory, and bone-forming functions. It accurately captures the diseased area flora in complex environments by responding to the inflammatory microenvironment. Additionally, the platform releases Mn nanozyme in response to acid, which catalyzes the production of O_2 from endogenous H_2O_2. This process works with Pae to regulate macrophage function

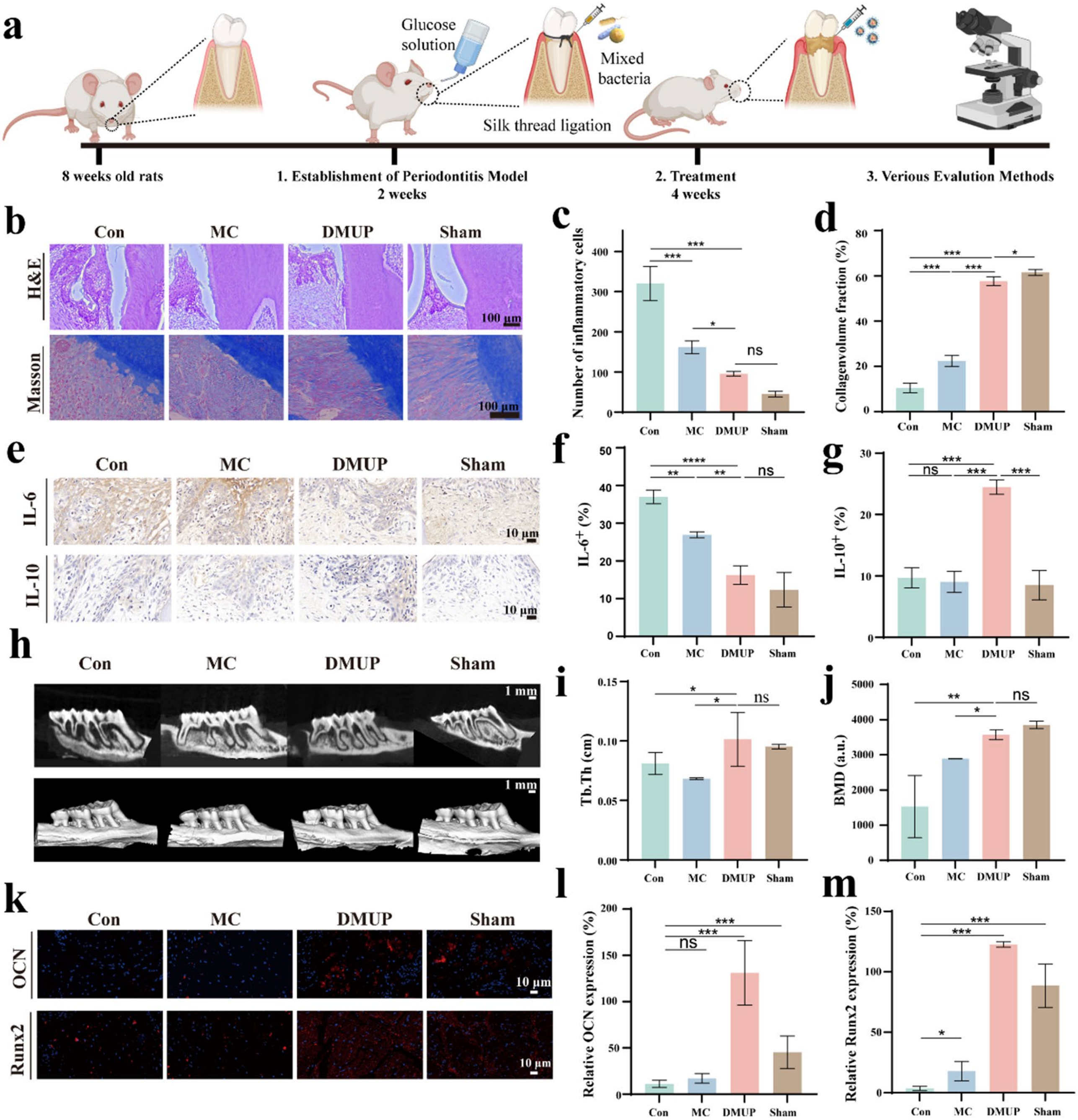

Fig. 9 In vivo assessment of anti-inflammatory osteogenic effect in animals. (**a**) Schematic diagram of periodontitis modeling on the maxillary left side of SD rats. Created with BioRender. (**b**) H&E and Masson staining of maxillary left side tissues of different groups after treatment, and (**c**) quantification of the number of inflammatory cell infiltration and (**d**) collagen content of periodontal tissues. (**e**) Representative images of tissue immunohistochemistry for positive expression of IL-6 and IL-10, and (**f**, **g**) quantitative results of positive expression. (**h**) Representative images of Micro-CT of maxillary left jaw after treatment in different groups, (**i**) Tb.Th parameters and (**j**) BMD values. (**k**) Immunofluorescence staining images of osteogenesis-related proteins OCN and Runx2 in tissue and (**l**, **m**) quantification results. Data are means ± s.d. ($n = 6$), ns: no significant difference, *$p < 0.05$, **$p < 0.01$, ***$p < 0.001$, ****$p < 0.0001$

and reduces the inflammatory factor content, resulting in improved periodontitis treatment outcomes. To further demonstrate the effectiveness of imaging infected areas in larger tissues, we verified the performance of DMUP, not only in an animal periodontitis model, but also in imaging bacterially infected areas in the legs of rats. This paves the way for potential application in treating larger tissue volumes. However, the system has limitations. First, the complex synthesis methods of materials pose a challenge for future large-scale production and in vivo metabolism. Second, in clinical applications, larger infected areas require treatment with scaling. Additionally, considering the complex flora in the oral environment, the effectiveness of combined treatment still needs further verification. Nevertheless, the combination of bacterial imaging and nanozyme for periodontitis is extremely significant and can be extended to the localization and treatment of other bacterial infectious diseases, such as various types of implants, bone plates, artificial joints, and vascular scaffolds.

Abbreviations

DMUP	β-NaErF$_4$:Yb^{3+}@NaLuF$_4$@mSiO$_2$-Mn-UBI$_{29-41}$-Pae
UBI$_{29-41}$	Ubiquicidin$_{29-41}$
Mn	Manganese
Pae	Paeonol
NIR-IIb	Near-infrared-IIb
ROS	Reactive oxygen species
SPR	Subgingival scaling and root planning
P. gingivalis	Porphyromonas gingivalis
MC	Minocycline
FRET	Fluorescence resonance energy transfer
NIR-II	Near-infrared-II
DCNPs	Down-conversion nanoparticles
PG	Phosphatidylglycerol
H_2O_2	Hydrogen peroxide
CAT	Catalase
O_2	Oxygen
SOD	Superoxide dismutase
$\cdot O_2^-$	Superoxide anion
mSiO$_2$	Mesoporous silica
ZIF-8	Zeolitic imidazolate framework
H^+	Hydrogen ions
DMU	β-NaErF$_4$:Yb^{3+}@NaLuF$_4$@mSiO$_2$-Mn-UBI$_{29-41}$
Re(CH$_3$CO$_2$)$_3$	Lanthanum acetate
OA	Oleic acid
ODE	1-octadecene
RT	Room temperature
NH$_4$F	Ammonium fluoride
NaOH	Sodium hydroxid
min	Minutes
Lu(CH$_3$CO$_2$)$_3$·xH$_2$O	Lutetium (III) acetate hydrate
CTAB	Cetyltrimethylammonium bromide
TEOS	Tetraethoxysilane
CHNaOSi	Carboxyethylsilanetriol sodium salt
HOBT	1-Hydroxybenzotriazole
EDC	1-Ethyl-3-(3-dimethylaminopropyl) carbodiimide hydrochloride
Zn(NO$_3$)$_2$·6H$_2$O	Zinc nitrate hexahydrate
KMnO$_4$	Potassium permanganate
DCFH-DA	2,7-dichlorodihydrofluorescein diacetate
Micro-CT	Micro-computed tomography
BV/TV	The bone volume per tissue volume
Tb. Th	trabecular Thickness
DM	DCMS-Mn
NCL	Native chemical ligation
XRD	X-ray diffraction
UV-vis	Ultraviolet-visible spectroscopy
XPS	X-ray photoelectron spectroscopy
FTIR	Fourier transform infrared
ICP-MS	Inductively coupled plasma-mass spectrometry
ESR	Electron spin resonance
CCK-8	Cell counting kit-8
[Ru(dpp)$_3$]Cl$_2$	Tris (4,7-diphenyl-1,10-phenanthroline) ruthenium (II) dichloride
FITC	Fluorescein isothiocyanate
fimA	Fimbrial protein A
kgp	Keratinsulfate glycoprotein
rgpA	Arginine-specific gingipain A
rgpB	Arginine-specific gingipain B
NF-κB	Nuclear factor kappa-light-chain-enhancer of activated B cells
MAPK	Mitogen-activated protein kinase
qRT-PCR	Quantitative real-time Polymerase chain reaction
TNF-α	Tumor necrosis factor-α
IL-1β	Transforming growth factor-β
IL-6	Interleukin-6
TGF-β	Transforming growth factor-β
iNOS	Inducible nitric oxide synthase
Arg-1	Arginase 1
IF	Immunofluorescence
CD86	Cluster of differentiation 86
CD206	Cluster of differentiation 206
PC	Principal component
GO	Gene ontology
DEGs	Differentially expressed genes
KEGG	Kyoto encyclopedia of genes and genomes
PI3k-Akt	Phosphoinositide 3-kinase-protein kinase B
mTOR	Mechanistic target of rapamycin
TNF	Tumor necrosis factor
Akt/mTOR	Akt/mechanistic target of rapamycin
mTORC1	Mechanistic target of rapamycin complex 1
MDC	Monodansylcadaverine
WB	Western blot
ULK1	Unc-51 like autophagy activating kinase 1
ATG16	Autophagy related 16
ATG5	Autophagy related 5
LC3II/LC3I	Microtubule-associated protein 1 A/1B-light chain 3 isoform II/microtubule-associated protein 1 A/1B-light chain 3 isoform I
MC3T3-E1	Mouse embryonic osteoblast precursor
ALP	Alkaline phosphatase
ARS	Alizarin Red Staining
COL-1	Collagen type I
Runx2	Runt-related transcription factor 2
OPN	Osteopontin
H&E	Hematoxylin-eosin
Con	Control
AL	Attachment loss
ABC	Alveolar bone crest
CEJ	Cementoenamel junction
BMD	Bone mineral density
HUVECs	Human umbilical vein endothelial cells
L929	Mouse fibroblast cells NCTC clone 929

Supplementary Information

The online version contains supplementary material available at https://doi.org/10.1186/s12951-025-03270-9.

Supplementary Material 1

Acknowledgements

Not applicable.

Author contributions

X. W. and J. Q. guided the project. X. W., J. Q. and S. L. conceived the idea and conceptualized the manuscript. T. C. and Y. J contributed equally to this work. S. L., T. C., Y. J., J. X., D. Z., J. J., D. D., M. Z., C. X., S. G., J. Q. and X. W. participated in the design of experimental methods and sample analysis. S. L. completed the processing of experimental data and wrote the manuscript. X. W. reviewed and edited the manuscript. All authors have given approval to the final version of the manuscript.

Funding

This research was supported by the Key Research and Development Program of Jiangxi Province (20212BBG73004 to Xiaolei Wang), the Interdiscipline Innovation Fund Project of Nanchang University (PYJX20230001 to Xiaolei Wang), Jiangxi Province Key Laboratory of bioengineering drugs (2024SSY07061 to Xiaolei Wang), the National Natural Science Foundation of China (82260194 to Jiaxuan Qiu), the Key Research and Development

Program of Science and Technology Department of Jiangxi Province (20212BBG71005 to Jiaxuan Qiu), the Science and Technology Innovation Base Construction Project of Science and Technology Department of Jiangxi Province (20221ZDG020068 to Jiaxuan Qiu), the Jiangxi Natural Science Foundation (20232BAB216073 to Jiaxuan Qiu), and the Key Projects of Jiangxi Administration of Traditional Chinese Medicine (GZY-KJS-2023-028 to Jiaxuan Qiu), the Graduate Innovation Special Fund Projects of Jiangxi Province (YC2023-B052 to Suai Lin).

Data availability
No datasets were generated or analysed during the current study.

Declarations

Ethics approval and consent to participate
The experimental procedures were carried out accordingly with the institutional guidelines for animal care and approved by the animal ethics committee of Nanchang University (Nanchang, China, NCULAE-20221228041).

Consent for publication
All authors agree to be published.

Competing interests
The authors declare no competing interests.

Author details
[1]Department of Oral and Maxillofacial Surgery, The First Affiliated Hospital, Nanchang University, Nanchang, Jiangxi 330006, P. R. China
[2]Jiangxi Provincial Key Laboratory of Oral Diseases, Department of Stomatology, The First Affiliated Hospital, Jiangxi Medical College, Nanchang University, Nanchang, Jiangxi 330006, P. R. China
[3]The National Engineering Research Center for Bioengineering Drugs and the Technologies, Institute of Translational Medicine, Nanchang University, Nanchang, Jiangxi 330088, P. R. China
[4]School of Chemistry and Chemical Engineering, Nanchang University, Nanchang, Jiangxi 330088, P. R. China

Received: 30 December 2024 / Accepted: 24 February 2025

References

1. Jakubovics NS, Goodman SD, Mashburn-Warren L, Stafford GP, Cieplik F. The dental plaque biofilm matrix. Periodontol 2000. 2021;86:32–56. https://doi.org/10.1111/prd.12361.
2. Peres MA, Macpherson LMD, Weyant RJ, Daly B, Venturelli R, Mathur MR, Listl S, Celeste RK, Guarnizo-Herreño CC, Kearns C, Benzian H, Allison P, Watt RG. Oral diseases: a global public health challenge. Lancet. 2019;394:249–60. https://doi.org/10.1016/S0140-6736(19)31146-8.
3. Sanz M, Herrera D, Kebschull M, Chapple I, Jepsen S, Berglundh T, Sculean A, Tonetti MS. EFP workshop participants and methodological consultants. Treatment of stage I–III periodontitis—the EFP S3 level clinical practice guideline. J Clin Periodontol. 2020;47:4–60. https://doi.org/10.1111/jcpe.13290.
4. Loesche WJ, Gusberti F, Mettraux G, Higgins T, Syed S. Relationship between oxygen tension and subgingival bacterial flora in untreated human periodontal pockets. Infect Immun. 1983;42:659–67. https://doi.org/10.1128/iai.42.2.659-667.1983.
5. Zhou M, Graves DT. Impact of the host response and osteoblast lineage cells on periodontal disease. Front Immunol. 2022;13:998244. https://doi.org/10.3389/fimmu.2022.998244.
6. Tan L, Li J, Liu XM, Cui ZD, Yang XJ, Zhu SL, Li ZY, Yuan XB, Zheng YF, Yeung KWK, Pan HB, Wang XB, Wu SL. Rapid biofilm eradication on bone implants using red phosphorus and near-infrared light. Adv Mater. 2018;30:1801808. https://doi.org/10.1002/adma.201801808.
7. Lin SC, Cheng Y, Zhang H, Wang XY, Zhang YY, Zhang YJ, Miao LY, Zhao XZ, Wei H. Copper Tannic acid coordination nanosheet: a potent nanozyme for scavenging ROS from cigarette smoke. Small. 2020;16:1902123. https://doi.org/10.1002/smll.201902123.
8. Shan C, Xia YN, Wu ZY, Zhao J. HIF-1α and periodontitis: novel insights linking host-environment interplay to periodontal phenotypes. Prog Biophys Mol Biol. 2023;184:50–78. https://doi.org/10.1016/j.pbiomolbio.2023.09.002.
9. Pampani P, Shenoy S, Punj A, Kamath VB. Comparison of oxidant stress levels among healthy, chronic periodontitis, and ischemic heart disease subjects with presence or absence of chronic periodontitis. Contemp Clin Dent. 2021;12:157–63. https://doi.org/10.4103/ccd.ccd_192_20.
10. Wang C, Zhao Q, Chen C, Li JJ, Zhang J, Qu SY, Tang H, Zeng H, Zhang YF. CD301b + macrophage: the new booster for activating bone regeneration in periodontitis treatment. Int J Oral Sci. 2023;15:19. https://doi.org/10.1038/s41368-023-00225-4.
11. Joshi N, Yan J, Levy S, Bhagchandani S, Slaughter KV, Sherman NE, Amirault J, Wang YF, Riegel L, He XY, Rui TS, Valic M, Vemula PK, Miranda OR, Levy O, Gravallese EM, Aliprantis AO, Ermann J, Karp JM. Towards an arthritis flare-responsive drug delivery system. Nat Commun. 2018;9:1275. https://doi.org/10.1038/s41467-018-03691-1.
12. Hu F, Zhou ZZ, Xu QC, Fan C, Wang L, Ren H, Xu S, Ji QX, Chen XG. A novel pH-responsive quaternary ammonium chitosan-liposome nanoparticles for periodontal treatment. Int J Biol Macromol. 2019;129:1113–9. https://doi.org/10.1016/j.ijbiomac.2018.09.057.
13. Gaber T, Strehl C, Buttgereit F. Metabolic regulation of inflammation. Nat Rev Rheumatol. 2017;13:267–79. https://doi.org/10.1038/nrrheum.2017.37.
14. Akhtar MS, Iqbal J, Khan MA, Irfanullah J, Jehangir M, Khan B, Ul-Haq I, Muhammad G, Nadeem MA, Afzal MS, Imran MB. 99mTc-labeled antimicrobial peptide Ubiquicidin (29–41) accumulates less in *Escherichia coli* infection than in *Staphylococcus aureus* infection. J Nucl Med. 2004;45:849–56.
15. Zhu YX, Luo XZ, Yu ZH, Wen SH, Bao GC, Zhang L, Zhang CL, Xian YZ. Dye-sensitized rare-earth-doped nanoprobe for simultaneously enhanced NIR-II imaging and precise treatment of bacterial infection. Acta Biomater. 2023;170:532–42. https://doi.org/10.1016/j.actbio.2023.08.051.
16. Yang R, Lou K, Wang P, Gao Y, Zhang Y, Chen M, Huang W, Zhang G. Surgical navigation for malignancies guided by near-infrared-II fluorescence imaging. Small Methods. 2021;5:2001066. https://doi.org/10.1002/smtd.202001066.
17. Huang YR, Chen WJ, Chung J, Yin J, Yoon J. Recent progress in fluorescent probes for bacteria. Chem Soc Rev. 2021;50:7725–44. https://doi.org/10.1039/D0CS01340D.
18. Alafeef M, Moitra P, Pan D. Nano-enabled sensing approaches for pathogenic bacterial detection. Biosens Bioelectron. 2020;165:112276. https://doi.org/10.1016/j.bios.2020.112276.
19. Sun LL, Shi SS, Geng HC, Huang Y, Qiao Y, Song J, Yang L, Grimes CA, Feng XX, Cai QY. NaGdF$_4$:Nd@NaGdF$_4$ core-shell down-conversion nanoparticles as NIR-II fluorescent probes for targeted imaging of bacteria. ACS Appl Nano Mater. 2021;4:11231–8. https://doi.org/10.1021/acsanm.1c02769.
20. Zasloff M. Antimicrobial peptides of multicellular organisms. Nature. 2002;415:389–95. https://doi.org/10.1038/415389a.
21. Hancock RE. Cationic peptides: effectors in innate immunity and novel antimicrobials. Lancet Infect Dis. 2001;1:156–64. https://doi.org/10.1016/S1473-3099(01)00092-5.
22. Jiang HJ, Cao ZP, Liu Y, Liu R, Zhou Y, Liu JY. Bacteria-based living probes: Preparation and the applications in bioimaging and diagnosis. Adv Sci. 2024;11:2306480. https://doi.org/10.1002/advs.202306480.
23. Kwon H, Liu X, Choi EG, Lee JY, Choi S, Kim J, Wang L, Park S, Kim B, Lee Y, Kim J, Kang NY, Chang Y. Development of a universal fluorescent probe for Gram-positive bacteria. Angew Chem Int Ed. 2019;58:8426–31. https://doi.org/10.1002/anie.201902537.
24. Wu HB, Wei M, Hu S, Cheng P, Shi SH, Xia F, Xu LN, Yin LN, Liang G, Li FY, Ling DS. A photomodulable bacteriophage-spike nanozyme enables dually enhanced biofilm penetration and bacterial capture for photothermal-boosted catalytic therapy of MRSA infections. Adv Sci. 2023;10:2301694. https://doi.org/10.1002/advs.202301694.
25. Chen MM, Song JT, Zhu JL, Hong GB, An J, Feng E, Peng XJ, Song FL. A dual-nanozyme-catalyzed cascade reactor for enhanced photodynamic oncotherapy against tumor hypoxia. Adv Healthc Mater. 2021;10:2101049. https://doi.org/10.1002/adhm.202101049.
26. Sun XL, Sun J, Sun Y, Li CY, Fang J, Zhang TS, Wan Y, Xu L, Zhou YM, Wang L, Dong B. Oxygen self-sufficient nanoplatform for enhanced and selective antibacterial photodynamic therapy against anaerobe-induced periodontal disease. Adv Funct Mater. 2021;31:2101040. https://doi.org/10.1002/adfm.202101040.
27. Ai YJ, You JZ, Gao JY, Wang JP, Sun H, Ding MY, Liang QL. Multi-shell nanocomposites based multienzyme mimetics for efficient intracellular antioxidation. Nano Res. 2021;14:2644–53. https://doi.org/10.1007/s12274-020-3267-x.

28. Fan RR, Chuan D, Liu ZY, Chen HX, Chen CL, Guo G, Xu JG. Antioxidant MnO_2 nanozymes-encapsulated hydrogel synergistically regulate the spinal ROS microenvironment and promote spinal cord repair. Chem Eng J. 2023;478:147148. https://doi.org/10.1016/j.cej.2023.147148.
29. Gao LK, Wang Z, Lu DH, Huang JL, Liu J, Hong L. Paeonol induces cytoprotective autophagy via blocking the Akt/mTOR pathway in ovarian cancer cells. Cell Death Dis. 2019;10:609. https://doi.org/10.1038/s41419-019-1849-x.
30. Tan QQ, Kong WS, Sun H, Qin X, Qu FL. Fluorometric turn-on detection of ascorbic acid based on controlled release of polyallylamine-capped gold nanoclusters from MnO_2 nanosheets. Microchim Acta. 2019;186:282. https://doi.org/10.1007/s00604-019-3399-4.
31. Wang MX, Zhou X, Li YH, Dong YQ, Meng JS, Zhang S, Xia LB, He ZZ, Ren L, Chen ZW, Zhang XC. Triple-synergistic MOF-nanozyme for efficient antibacterial treatment. Bioact Mater. 2022;17:289–99. https://doi.org/10.1016/j.bioactmat.2022.01.036.
32. Luo XY, Cao J, Yu JM, Dai DQ, Jiang W, Feng YH, Hu Y. Regulating acidosis and relieving hypoxia by platelet membrane-coated nanoparticle for enhancing tumor chemotherapy. Front Bioeng Biotechnol. 2022;10:885105. https://doi.org/10.3389/fbioe.2022.885105.
33. Chiang W, Hu Y, Liu H, Hsiao C, Sureshbabu R, Yang C, Chung M, Chia W, Sung H. Injectable microbeads with a thermo-responsive shell and a pH-responsive core as a dual-switch-controlled release system. Small. 2014;10:4100–5. https://doi.org/10.1002/smll.201400842.
34. Koppolu P, Sirisha S, Penala S, Reddy PK, Alotaibi DH, Abusalim GS, Lingam AS, Mukhtar AH, Barakat A, AlMokhatieb AA. Correlation of blood and salivary pH levels in healthy, gingivitis, and periodontitis patients before and after non-surgical periodontal therapy. Diagnostics. 2022;12:97. https://doi.org/10.3390/diagnostics12010097.
35. Niu YZ, Jin YY, Hao YX, Liang W, Tang F, Qin ZY, Liang T, Shi L. Paeonol interferes with lupus nephritis by regulating M1/M2 polarization of macrophages. Mol Immunol. 2024;169:66-77. https://doi.org/10.1016/j.molimm.2024.03.004
36. Huang K, Liu WB, Wei WY, Zhao YN, Zhuang PZ, Wang XX, Wang YF, Hu YH, Dai HL. Photothermal hydrogel encapsulating intelligently bacteria-capturing bio-MOF for infectious wound healing. ACS Nano. 2022;16:19491–508. https://doi.org/10.1021/acsnano.2c09593.
37. Bi ZG, Cai YM, Shi XT, Chen JT, Li DS, Zhang PB, Liu JG. Macrophage-mediated Immunomodulation in biomaterial-assisted bone repair: molecular insights and therapeutic prospects. Chem Eng J. 2024;488:150631. https://doi.org/10.1016/j.cej.2024.150631.
38. Jiang JK, Xie JL, Zhou L, Han W, Ye J, Hu DR, Xie WC, Qiu JB, Chen RF, Wang XL. Near infrared responsive nitric oxide and carbon monoxide nanoplatform for synergistic photodynamic therapy against periodontitis. Chem Eng J. 2024;480:147850. https://doi.org/10.1016/j.cej.2023.147850.
39. Diemer V, Ollivier N, Leclercq B, Drobecq H, Vicogne J, Agouridas V, Melnyk O. A cysteine Selenosulfide redox switch for protein chemical synthesis. Nat Commun. 2020;11:2558. https://doi.org/10.1038/s41467-020-16359-6.
40. Ye YL, Sun XY, Zhang YZ, Han XM, Sun XL. A novel cell-based electrochemical biosensor based on MnO_2 catalysis for antioxidant activity evaluation of anthocyanins. Biosens Bioelectron. 2022;202:113990. https://doi.org/10.1016/j.bios.2022.113990.
41. Yang B, Pang XF, Li ZP, Chen ZF, Wang Y. Immunomodulation in the treatment of periodontitis: progress and perspectives. Front Immunol. 2021;12:781378. https://doi.org/10.3389/fimmu.2021.781378.
42. Mendes RT, Nguyen D, Stephens D, Pamuk F, Fernandes D, Hasturk H, Van Dyke TE, Kantarci A. Hypoxia-induced endothelial cell responses– possible roles during periodontal disease. Clin Exp Dent Res. 2018;4:241–8. https://doi.org/10.1002/cre2.135.
43. Watts ER, Howden AJM, Morrison T, Sadiku P, Hukelmann J, Von Kriegsheim A, Ghesquiere B, Murphy F, Mirchandani AS, Humphries DC, Grecian R, Ryan EM, Coelho P, Blanco GR, Plant TM, Dickinson RS, Finch A, Vermaelen W, Cantrell DA, Whyte MK, Walmsley SR. Hypoxia drives murine neutrophil protein scavenging to maintain central carbon metabolism. J Clin Invest. 2021;131:e134073. https://doi.org/10.1172/JCI134073.
44. Chen QH, Qi ML, Shi FY, Liu CY, Shi YJ, Sun Y, Bai X, Wang L, Sun XL, Dong B, Li CY. Novel twin-crystal nanosheets with MnO_2 modification to combat bacterial biofilm against periodontal infections via multipattern strategies. Adv Healthc Mater. 2023;12:2300313. https://doi.org/10.1002/adhm.202300313.
45. Dai XJ, Bai YY, Zhang YF, Ma Z, Li J, Sun HN, Zhang XG. Protonation–activity relationship of bioinspired ionizable glycomimetics for the growth Inhibition of bacteria. ACS Appl Bio Mater. 2020;3:3868–79. https://doi.org/10.1021/acsabm.0c00424.
46. Li LY, Gu PL, Hao MQ, Xiang XL, Feng YT, Zhu XK, Song Y, Song E. Bacteria-targeted MRI probe-based imaging bacterial infection and monitoring antimicrobial therapy *in vivo*. Small. 2021;17:2103627. https://doi.org/10.1002/smll.202103627.
47. Johnston W, Rosier BT, Artacho A, Paterson M, Piela K, Delaney C, Brown JL, Ramage G, Mira A, Culshaw S. Mechanical biofilm disruption causes microbial and immunological shifts in periodontitis patients. Sci Rep. 2021;11:9796. https://doi.org/10.1038/s41598-021-89002-z.
48. El-Kenawi A, Ruffell B. Inflammation, ROS, and mutagenesis. Cancer Cell. 2017;32:727–9. https://doi.org/10.1016/j.ccell.2017.11.015.
49. Wang FJ, Yuan HT, Shen J, Li ZJ, Li JX, Luo P, Zhang Q, Huang W, Wang XX, Ma JB, Zhang WQ, Fu CJ, Sun JC, Sun X, Wang JG, Xiao W. Nanozymes with broad-spectrum scavenging of reactive oxygen species (ROS) alleviate inflammation in acute liver injury. ACS Mater Lett. 2024;6:1304–16. https://doi.org/10.1021/acsmaterialslett.3c01627.
50. Bao XF, Zhao JH, Sun J, Hu M, Yang XR. Polydopamine nanoparticles as efficient scavengers for reactive oxygen species in periodontal disease. ACS Nano. 2018;12:8882–92. https://doi.org/10.1021/acsnano.8b04022.
51. Guo YR, Ding S, Shang CS, Zhang CG, Li MG, Zhang QH, Gu L, Heng BC, Zhang SH, Mei F, Huang Y, Zhang XH, Xu MM, Jiang JH, Guo SJ, Deng XL, Chen LL. Multifunctional PtCuTe nanosheets with strong ROS scavenging and ROS-independent antibacterial properties promote diabetic wound healing. Adv Mater. 2024;36:2306292. https://doi.org/10.1002/adma.202306292.
52. Matsuzawa-Ishimoto Y, Hwang S, Cadwell K. Autophagy and inflammation. Annu Rev Immunol. 2018;36:73–101. https://doi.org/10.1146/annurev-immunol-042617-053253.
53. Wang SF, Wang PY, Thompson R, Ostrikov K, Xiao Y, Zhou YH. Plasma-activated medium triggers Immunomodulation and autophagic activity for periodontal regeneration. Bioeng Transl Med. 2023;8:e10528. https://doi.org/10.1002/btm2.10528.
54. Xing MY, Bian S, Li BB, Wei M, Yang ZM, Li JJ. Functional peptide hydrogel for the synergistic treatment of atherosclerosis based on macrophage autophagy induction and anti-inflammation. ACS Mater Lett. 2024;6:384–99. https://doi.org/10.1021/acsmaterialslett.3c01285.
55. Zhang WT, Lu HD, Zhang WY, Hu JH, Zeng YF, Hu HQ, Shi LY, Xia JY, Xu F. Inflammatory microenvironment-responsive hydrogels enclosed with quorum sensing inhibitor for treating post-traumatic osteomyelitis. Adv Sci. 2024;11:2307969. https://doi.org/10.1002/advs.202307969.
56. Pan HJ, Miao XX, Deng JJ, Pan CZ, Cheng XG, Wang XL. Bimetallic metal–organic framework for mitigating aseptic osteolysis. ACS Appl Mater Interfaces. 2023;15:4935–46. https://doi.org/10.1021/acsami.2c19449.
57. Gaharwar AK, Mihaila SM, Swami A, Patel A, Sant S, Reis RL, Marques AP, Gomes ME, Khademhosseini A. Bioactive silicate nanoplatelets for osteogenic differentiation of human mesenchymal stem cells. Adv Mater. 2023;35:2300774. https://doi.org/10.1002/adma.202300774.
58. Papapanou PN, Susin C. Periodontitis epidemiology: is periodontitis under-recognized, over-diagnosed, or both? Periodontol 2000. 2017;75:45–51. https://doi.org/10.1111/prd.12200.

Publisher's note